On the response of a turbulent coastal buoyant current to wind events: the case of the Western Adriatic Current

M. G. Magaldi [a,*], T. M. Özgökmen [a], A. Griffa [a,b], M. Rixen [c]

[a] *Rosenstiel School of Marine and Atmospheric Science/MPO, Univ. of Miami, 4600 Rickenbacker Cswy, Miami, Florida, 33149-1098, USA*

[b] *Istituto di Scienze Marine, Consiglio Nazionale delle Ricerche, Forte Santa Teresa, I-19036, Pozzuolo di Lerici (SP), Italy*

[c] *NURC, NATO Undersea Research Centre, Viale San Bartolomeo 400, I-19126, La Spezia (SP), Italy*

Abstract

This numerical study focuses on the response of the Western Adriatic Current to wind forcing. The turbulent buoyant surface current is induced by the Po river outflow in the Adriatic Sea. Idealized and realistic wind conditions are considered by retaining the complex geomorphology of the middle Adriatic basin.

In the absence of wind, the Adriatic Promontories force the current to separate from the coast and induce instabilities. Persistent 7 m sec^{-1} downwelling favorable northwesterly winds thicken and narrow the current. Instabilities whose size is ~ 10 km develop but ultimately vanish, since there is not enough across-shore space to grow. On the contrary, 7 m sec^{-1} upwelling favorable southeasterly winds thin and widen the current, and instabilities can grow to form mesoscale (~ 35 km) features. When realistic winds are considered, the same trends are observed, but the state of the sea set up by previous wind events plays also a crucial role.

The turbulent regimes set up by different winds affect mixing and the WAC meridional transport. With downwelling winds the transport is generally southward and mixing happens mostly between the fresher ($S \leq 38$) salinity classes. With upwelling winds, the transport decreases and changes sign, and mixing mainly involves saltier ($S > 38$) waters. In all cases mixing is enhanced when a finer 0.5 km horizontal resolution is employed.

Key words: Mesoscale variability; Adriatic Sea; Western Adriatic Current; Instabilities; Gargano Promontory; Cape; Transport; Mixing.

1 Introduction

A large number of studies have focused on the role of the intensity and direction of winds in influencing the fate of coastal buoyant currents (Chao, 1987, 1988; Blanton et al., 1989; Münchow and Garvine, 1993; Kourafalou et al., 1996; Fong et al., 1997; Xing and Davies, 1999; Fong and Geyer, 2001; Lentz, 2001; Whitney and Garvine, 2005; Lentz and Largier, 2006). Due to Ekman dynamics, upwelling favorable winds thin, widen and decelerate coastal currents. If winds persist for several days, they can reverse the flow and force lighter waters to separate from the coast and move offshore (e.g. Fong and Geyer, 2001). On the contrary, moderate downwelling favorable winds thicken, narrow and speed up the current. If strong enough they can induce vertical mixing and steepen the plume front (e.g. Lentz and Largier, 2006).

These studies have focused on systems where the coastal current is assumed to be dynamically steady and not turbulent. However, satellite images show that coastal buoyant currents are usually characterized by instabilities (see Figures 9 and 12 of Sur et al. 1994, plate 1 of Cushman-Roisin et al. 2001, Figure 3 of Chanut et al. 2008). Meanders, squirts and eddies detach from the core of the current and affect the exchange of properties between different water masses. The understanding of their evolution, therefore, is of primary importance to assess mixing and transport of coastal waters. Even though satellite observations have related the emergence of instabilities to wind direction (Bignami et al., 2007), little attention has been paid to the role of the winds in modifying these disturbances.

This study is therefore performed to establish and understand which winds are able to enhance or suppress turbulent coherent structures, and what are the results of the modifications in terms of integral quantities. The middle portion of the Adriatic Sea is considered as a case study. In this case the coastal current is the Western Adriatic Current (herein after referred as WAC). The WAC is forced by the Po river runoff and the heating taking place in the northwestern part of the basin. The current hugs the eastern Italian coast flowing southeastward to finally exit the Adriatic basin via the Otranto Strait. During its path it has to follow a complex and tortuous coastline, characterized by the presence of two large capes, the Conero and Gargano Promontories (Fig. 1a).

There are two main reasons to consider the WAC as a case study. In general, different studies show that the Adriatic Sea is characterized by strong

---

* Corresponding author now at the Department of Earth and Planetary Sciences, The Johns Hopkins University, 328 Olin Hall, 34th and North Charles Streets, Baltimore, Maryland 21218, USA, *phone*: +1 410-516-0155, *fax*: +1 410-516-7933
  Email address: Marcello.Magaldi@jhu.edu (M. G. Magaldi).

Fig. 1. a) Geographic locations in the Adriatic Sea. The isobaths of 20 m, 40 m, 60 m, 80 m, 100 m, 200 m, 1000 m and 1200 m are also shown; Chlorophyll-A SeaWifs images (mg m^{-3}) processed by SeaDAS (see http://oceancolor.gsfc.nasa.gov/seadas/) using the OC4 algorithm (O'Reilly et al., 1998): b) August 12, 2001; c) August 14, 1998.

mesoscale activity (Cushman-Roisin et al., 2001; Korotenko, 2007; Barale et al., 1984; Paschini et al., 1993). In particular, satellite images show that the WAC state is variable. Sometimes the coastal current flows smoothly along the western side of the central and south Adriatic. In these cases, the only clear instabilities are localized in the lee of the Gargano Promontory, where isolated eddies can be recognized (Fig. 1b). Other times, the current is characterized by instabilities along its entire path (Fig. 1c). These instabilities

appear upstream and downstream of the topographic features and, due to the complexity of the system, the mechanisms controlling their variability remain unclear.

Furthermore, the middle Adriatic Sea represents an excellent case study since the area has been the focus of many experiments. In this study, the focus is on the data from the recent Dynamics of the Adriatic in Real Time (DART) project (see http://geos2.nurc.nato.int/ and Rixen et al. 2009a,b). The DART project was a comprehensive international effort aimed at monitoring and predicting in real-time the complex dynamics in the central Adriatic Sea. It involved the use of a wide range of data from different instruments and realistic numerical atmospheric and ocean models. The winter (DART06a) and summer (DART06b) periods were considered to assess seasonal variability.

The following main questions are addressed in this study: a) Is the WAC inherently stable or unstable when it flows along the complex topography of the middle Adriatic Sea? b) What is the role of the wind in stabilizing, destabilizing turbulent instabilities? c) How do the turbulent coherent structures evolve in the presence of different winds? d) How does this evolution affect integral quantities such as mixing and current transport?

The WAC state during the summer DART06b period has been recently under investigation. Satellite images, together with in situ data and operational model output, reveal changes in the mesoscale WAC activity in the order of days (Burrage et al., 2009). The DART06b time interval is therefore the ideal period to address the questions posed in this study. It remains difficult to answer these questions in studies which either observe the results of complex interactions or deal with the output of numerical operational models. A better understanding can be achieved through a process study which uses the data collected during the DART06b period in simplified scenarios. As better explained in section 2.3 of the paper, in order to reduce complexity, the simulations of this study are only boundary, buoyancy and wind driven. Other forcings used in operational models, like evaporation and precipitation rates, tidal motion, runoff of small Adriatic rivers and surface heat fluxes, are not considered. Furthermore, important large scale Adriatic features like the Levantine Intermediate Water, which flows at intermediate depths, are neglected in this process study since they do not have a direct impact in modifying surface instabilities.

In the first phase of the study, the WAC dynamics and the instability process are assessed without wind forcing. In order to simulate as realistically as possible the WAC evolution, the complex coastline and the topographic features of the western Adriatic are retained. In the second phase the role of winds is investigated. Idealized wind simulations based on typical wind speeds and directions of the DART06b summer period are first considered. High temporal

and spatial resolution realistic winds are then used to force more realistic runs. In the third phase the differences in the various cases are quantified. Specifically, integral quantities like WAC transport and mixing are considered.

It is found that with both downwelling and upwelling favorable winds the coastal current develops instabilities. In downwelling conditions, however, the current appears more steady since the instabilities are small ($\sim$ 10 km) and tend ultimately to disappear. In upwelling conditions, instead, they persist and grow to form mesoscale ($\sim$ 35 km) eddies. It is shown that the different dynamical regimes set up by winds affect mixing and alongshore current transport.

The paper is organized as follows: in section 2 the study area is presented. Particular attention is given to topography and wind forcing. The numerical setup for all the simulations is also described. Results for all the experiments are presented in section 3. Specifically, the implications of wind forcing in integral quantities like mixing and meridional transport are shown in sections 3.4 and 3.5. Finally, conclusions are given in section 4.

2   Method

2.1   Study area

The study area is located in the middle Adriatic Sea, along the Italian coast. The Western Adriatic Current mesoscale activity in the region varies depending on the season and on the year. In winter, the middle Adriatic WAC seems to be generally narrow and relatively smooth (Barale et al., 1984). In autumn, mesoscale baroclinic eddies are observed in moorings located along the Italian coast. Their diameter is estimated to be around 10-20 km and comparable to the local Rossby radius of deformation of the first baroclinic modes (Paschini et al., 1993). Similar structures have been successfully modeled in recent and realistic simulations of the Adriatic Sea (Cushman-Roisin et al., 2007; Korotenko, 2007). The same simulations also show that mesoscale features evolve and dissipate on time scales of the order of days or weeks. Understanding this variability remains a challenging task. It is already known that variations in the Po river discharge can produce unusual effects in the vicinity of promontories as documented by Poulain et al. (2004) and modeled by Korotenko (2007). Other factors like topography and winds can play a role in modifying the evolution of the turbulent features.

The Western Adriatic dynamics are strongly influenced by the geometry of the basin, in particular by the presence of promontories. Previous studies have

shown that instabilities can be associated with both Adriatic Promontories, Conero and Gargano. Turbulent structures like the so-called Rimini Squirt and the Triple Meanders appear respectively upstream and downstream of the Conero Promontory (Korotenko, 2007; Cushman-Roisin et al., 2007). Instabilities surround also the Gargano Promontory (Barale et al., 1984). Furthermore, surface drifter data and satellite images have also revealed a recirculation region in its lee (Poulain, 2001; Veneziani et al., 2007; Burrage et al., 2009).

Alongshore asymmetries are evident in Fig. 1a for both promontories. Waters remain shallow upstream of the Conero Promontory as in the whole north Adriatic basin. Downstream of the Promontory, waters follow the coastline and become deeper and deeper until they reach the Middle Adriatic Pit. As a result, the Conero Promontory downstream topography divides the shallow part of the basin from the rest. The shelf upstream of Gargano Promontory, instead, is well defined and extends up to the 200 m isobath until the Palagruza Sill. However, it widens downstream of the Promontory and the Gulf of Manfredonia is characterized by shallower waters of about 20 m. To further complicate the scenario, in the offshore downstream Gargano Promontory area, the South Adriatic Pit can be found. This abyssal depression reaches a depth of 1200 m and represents the deepest part of the whole Adriatic.

The fact that WAC instabilities can vary in short time periods of the order of days, suggests the possibility that wind forcing can play an important role. Different studies have already associated the changes in the character of WAC turbulence with wind variations. Bignami et al. (2007) have shown that the inhomogeneity in the Bora wind fields enhances instabilities in the northern Adriatic and increases the offshore transport of riverine waters. Poulain et al. (2004) have observed that, occasionally, Sirocco winds can induce the WAC to reverse its flow direction and cause unusual upwelling events along the Italian coast. These events are associated with convoluted filaments extending offshore. However, an understanding of how a peculiar wind direction enhances or suppresses the turbulent structures within the WAC is generally missing, and the analysis can benefit from further investigations.

A numerical study aimed at understanding the WAC variability needs to retain the interplay between the geometry of the basin and changes in wind forcing. In the following section, wind data used in this study are introduced, while the bathymetry is described with the numerical setup on section 2.3.

2.2 Wind forcing

The DART06b period begins on August 16, 2006 and ends on September 26 of the same year. Wind stress vectors for this period are obtained from
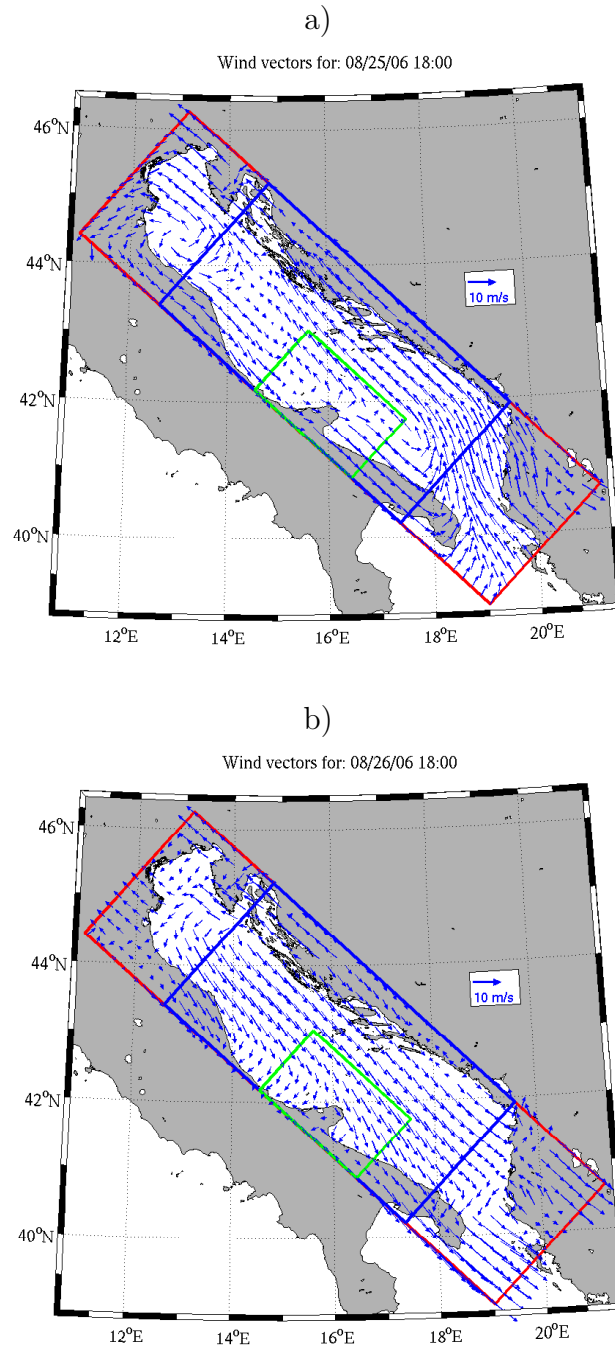
a)

b)

Fig. 2. Six-hour averaged wind vectors for August 2006; a) 25, 18:00; b) 26, 18:00. The boxes show the different areas considered for the spatial average.

the Aire Limitée Adaption dynamique Dévelopment InterNational (ALADIN) atmospheric model and are used to force operational numerical models (e.g. Martin et al., 2009). They have high spatial and temporal resolution ($\simeq$ 1 km, 1 hr) and cover the whole Adriatic basin (Fig. 2).

During the period considered, wind speed and direction can significantly change
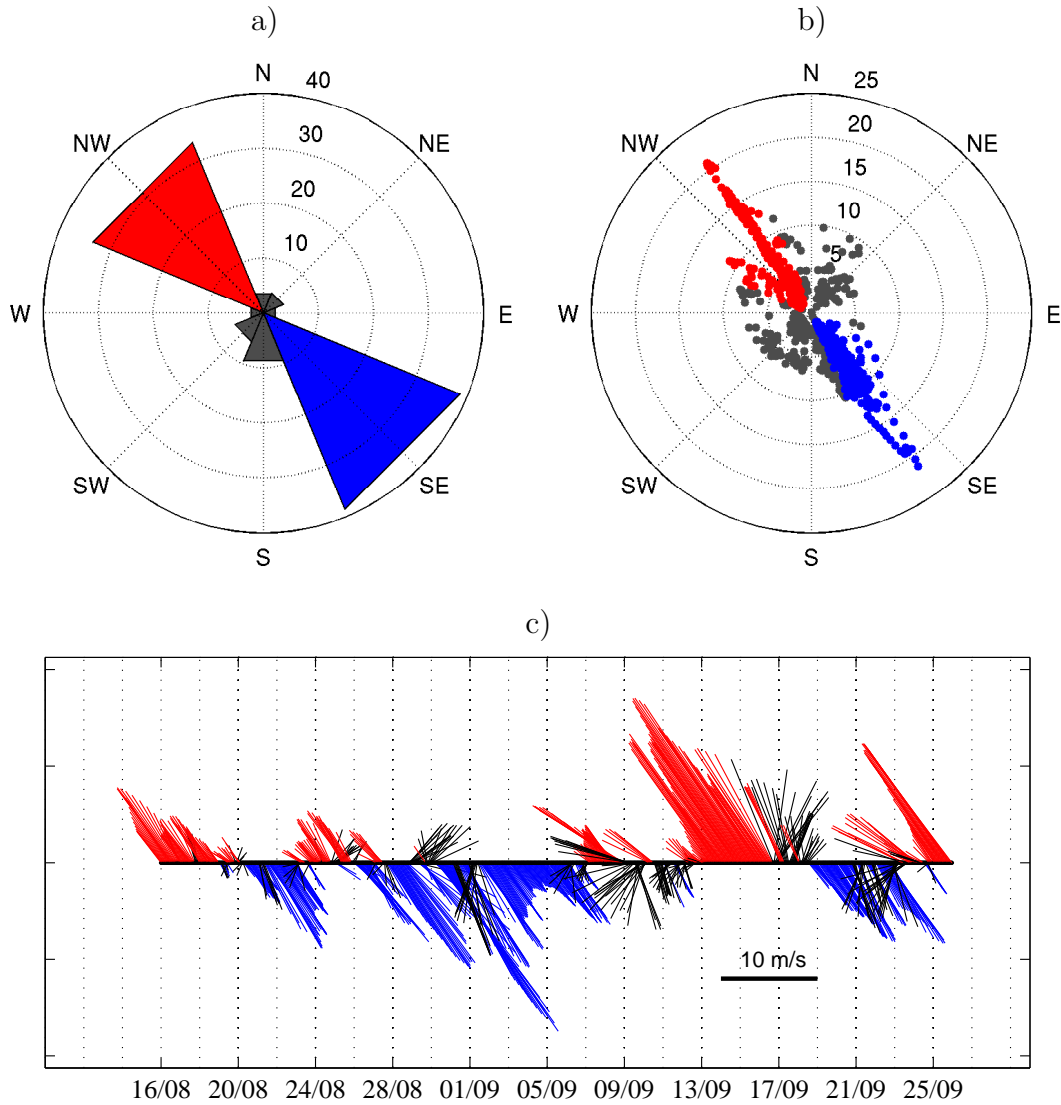
Fig. 3. Area averaged wind vectors for the period considered. a) Direction frequencies (%); b) Wind speed (m sec^{-1}) and direction; c) Wind stick plot for the DART06b period. Blue color stands for Mistral winds, red color for Sirocco.

on the order of days (cf Fig. 2a and b). Wind spatial variability is also high: winds along the Croatian coast can flow in the opposite direction of those close to the Italian coast (Fig. 2a). Furthermore, the presence of the Gargano Promontory seems to shield the lee of the Promontory and to create a typical wind shadow effect. This effect was recently recognized (Pasarić et al., 2009) and it is clearly visible in Fig. 2b.

In order to assess the dominant winds and the response to typical directions, spatial averages are calculated. Different areas have been considered for the

	Mean Direction (° from North)	Mean (m/sec)	Std. Dev. (m/sec)	Min (m/sec)	Max (m/sec)
Total	-	6.24	3.96	0.00	21.26
Mistral	145	6.95	3.42	1.20	21.26
Sirocco	321	7.09	4.84	1.31	20.76

Table 1
Statistics for the area-averaged winds.

average (Fig. 2) and the final results have been seen not to change significantly. Here only the results obtained averaging over the area enclosed in the blue rectangle of Fig. 2 are presented. Fig. 3a shows the averaged-wind frequency in this area for the different wind directions. The oceanographic convention is used, so each histogram represents the direction the winds blow toward. In the DART06b period, winds blow toward two prevalent directions: Mistral winds blowing toward southeast (northwesterly winds) appear for more than 35% of the time while Sirocco winds blowing toward northwest (southeasterly winds) are slightly less frequent (32%). Fig 3b is a scatter plot for wind speed in function of direction. It shows that only Mistral and Sirocco events are strong enough to exceed the value of 10 m sec^{-1}. The same two dominant directions are evident in the wind stick plot for the whole period considered (Fig. 3c). Particular emphasis should be given to two events. The first is the strongest Mistral event starting on August 30 and lasting for just two days. The other is the strongest Sirocco event starting on September 13 and lasting for almost four days. Bora winds blowing toward southwest (northeasterly winds) which are usually predominant in the Adriatic Sea, are weak in the DART06b period and just appear around September 10. This is consistent with previous studies. Bora events have a marked seasonality and usually almost disappear during the summer months (Bignami et al., 2007). As a result, Mistral winds dominate in summer (cf. Figure 4 of Bignami et al., 2007).

The basic statistics for the area-averaged winds are listed in Table 1. The mean speed value for both Mistral and Sirocco winds is close to 7 m sec^{-1}. This value represents a natural choice to setup idealized wind experiments which consider both prevalent wind directions (see Section 2.3 and Table 2). The total average in the whole period is influenced by weaker winds coming from other directions and it is slightly smaller. Mistral events are less variable in intensity than Sirocco ones. Finally, it is worthy noticing that both Mistral and Sirocco winds can be over 20 m sec^{-1}.

The evolution of the WAC is simulated using the Regional Ocean Modeling System (ROMS). ROMS is a free-surface terrain-following ocean model which solves the primitive equations based on the Boussinesq and hydrostatic approximations. ROMS uses the time-splitting technique where the barotropic vertically-averaged equations are integrated more frequently than the three-dimensional equations for temperature, salinity, and baroclinic momentum (Shchepetkin and McWilliams, 2005).

In this study, ROMS ability to run with zero explicit numerical viscosity is used. ROMS advection operator relies on the third-order, upstream-biased scheme described in detail in Shchepetkin and McWilliams (1998). The numerical viscosity implicit in such a scheme has been shown to avoid oscillatory behavior in the vicinity of steep gradients and to result in a weak mesh dependent dissipation. Thus, the explicit viscosity can be set to be zero allowing the solution to be enhanced by a given grid size while still ensuring stability. ROMS zero explicit viscosity is used in numerous works in the literature (e.g. Lutjeharms et al., 2003; Dong and McWilliams, 2007; Capet et al., 2008a,b; Magaldi et al., 2008; Silva et al., 2009) and has been shown to compare with simulations run with low viscosity values in the order of 0.625 m^2/sec (compare Fig. 9 and 10 of Dong et al., 2007). The advantage of this choice is to use the least possible amount of numerical dissipation, and to run at the largest affordable effective Reynolds number with a certain discretization in order to allow the growth of instabilities. Here it is worth noticing that, since the amount of numerical viscosity changes with the grid size, simulations at different resolutions run at different effective Reynolds numbers and are dynamically different by construction.

Different numerical modeling efforts aimed at simulating the circulation of the Adriatic Sea can be found in the literature. The various models run all in operational mode but with different characteristics (e.g. Rixen et al., 2009a). The Adriatic Sea Regional Model (AREG) is based on the Princeton Ocean Model, POM (Blumberg and Mellor, 1987) and runs on a regular horizontal grid of about 5 km resolution. AREG uses the Smolarkiewicz (1984) advection scheme and is forced with atmospheric data obtained from the European Centre for Medium Range Weather Forecasts (ECMWF) analysis, river discharges and lateral open boundary conditions. AREG studies are mainly concerned with the seasonal variability of the Adriatic circulation (Zavatarelli and Pinardi, 2003; Oddo et al., 2006). The DieCAST model is run with about 2 km resolution using a fourth-order accurate advection scheme (Cushman-Roisin et al., 2007; Cushman-Roisin and Korotenko, 2007). Atmospheric fluxes from the Coupled Ocean-Atmosphere Mesoscale Prediction System (COAMPS), open boundary conditions and freshwater fluxes are used to force the simulations.

The Navy Coastal Ocean Model (NCOM) is run at 1 km resolution using a third-order upwind advection scheme. Model forcing includes atmospheric fluxes, tides, open boundary conditions, river and runoff discharges. Atmospheric data sources can vary from COAMPS as in Martin et al. (2007) to ALADIN as in Martin et al. (2009). Both DieCAST and NCOM are shown to simulate and reproduce mesoscale Adriatic features observed above all in satellite images (Korotenko, 2007; Burrage et al., 2009).

A ROMS-based forecast system named AdriaROMS is also run on a variable grid ranging from 3 km in the north Adriatic to about 10 km in the south (Chiggiato and Oddo, 2008). AdriaROMS uses the above mentioned advection scheme of Shchepetkin and McWilliams (1998) and is forced by atmospheric data provided by the Limited Area Model Italy (LAMI), river discharges and open boundary conditions which include tides. A similar configuration but with a resolution of about 4 km, has been recently used to investigate the variability of turbid coastal waters in the Adriatic Sea (Bignami et al., 2007). Given the comparable weakly-diffusive scheme and the high resolution meshes used in this study (2 km and 0.5 km), ROMS is expected to perform as well as the other models in reproducing the mesoscale Adriatic features.

The Adriatic Sea topography is considered in a domain which is 530 km long and 230 km wide (Fig. 4a). The numerical grid is rotated 60° clockwise with respect to true North. The realistic topography retains all the important bathymetric features underlined previously. In particular, the reentrance of the coast downstream of the Conero Promontory and the asymmetries across the Gargano Promontory are evident in Fig. 4a. A three-dimensional close up near the Gargano Promontory is shown in Fig. 4b. Note the downstream depression of the South Adriatic Pit.

The vertical dimension is discretized by 30 sigma layers. Since the focus is on surface instabilities, the layers are unevenly spaced in the vertical and gathered at the top of the water column. All simulations are run with the ROMS default generic length scale algorithm (Umlauf and Burchard, 2003) which defines a $k - \varepsilon$ turbulence closure with Canuto-A stability functions (Canuto et al., 2001). The bottom stress is calculated directly by the model according to the quadratic relation $\vec{\tau}_b = -\rho_o C_D \, \vec{v}_b \sqrt{u_b^2 + v_b^2}$, where $\vec{v}_b \equiv (u_b, v_b)$ is the velocity at the middle of the bottom cell, ρ_o the water density and $C_D = 3 \times 10^{-3}$ the bottom drag coefficient. The base experiment has a uniform horizontal resolution of $\Delta x = \Delta y = 2$ km. The baroclinic timestep is $\Delta t = 300$ sec and the simulation is run for five months until it reaches a plateau in the kinetic energy (see section 3.1, Fig. 5 and 6 for a better discussion).

Open boundaries are located south and north of the domain while a no-slip condition is implemented at eastern and western boundaries (the Italian and Croatian coasts, respectively). Since the focus is only on the surface western

Adriatic circulation, the base simulation starts at rest and is forced by inflow conditions at the open boundaries which simulate the Adriatic climatological mass fluxes. The initial salinity and temperature fields vary only with depth according to hyperbolic tangent profiles. The surface and bottom initial values are respectively $S^{srf} = 38.3$, $T^{srf} = 23.5°C$ and $S^{bot} = 38.5$, $T^{bot} = 13.0°C$. During summer, the Po river waters are mainly characterized and recognizable by low salinity values. The WAC temperature signal almost disappears as riverine and sea temperatures are similar. Therefore, the initial temperature profile is held constant in time and the inflow of riverine waters at the northern boundary is simulated by nudging the salinity field in an area 48 km long. In this area, the salinity is relaxed to analytical profiles obtained by fitting the northern hydrological data collected at the beginning of the DART06b period to hyperbolic tangent functions (see Appendix). As a result, the salinity is assigned near the coast to the value of $S^{srf}_{min} = 37.2$ in an area 8 km wide. Moving offshore it gradually increases following an exponential behavior with a length scale of 12 km. The exact definitions of the initial and boundary tracer profiles are given in the Appendix.

The northern barotropic inflow velocity V_N is assumed to be made up of two contributions $V_N = V_N^c + V_N^p$. The first one is due to the general cyclonic circulation of the basin while the second to the presence of the buoyant plume. V_N^c is prescribed in order to obtain a general cyclonic transport of ∓0.15 Sv at the northwestern and northeastern corners, respectively. This value is close to the average value of 0.147 Sv measured by Book et al. (2007) from October 2002 trough April 2003 in the same area.

For the flow due only to density gradients, the thermal wind equation is used to calculate the inflow velocity profile

$$v_N^p(x,z) = \int_{-H}^{z} \frac{\partial v}{\partial z} dz = -\frac{g}{f\rho_o} \int_{-H}^{z} \frac{\partial \rho}{\partial x} dz, \qquad (1)$$

where ρ is the density field, ρ_o is the average density value in the domain, $H(x,y)$ the bottom, g the gravitational acceleration and f the Coriolis parameter. V_N^p is then obtained vertically averaging equation (1).

At the southern boundary, V_S is prescribed in order to obtain a general cyclonic transport of ∓1.0 Sv at the southwestern and southeastern corners, respectively. This transport is estimated by the summer and annual average of Strait of Otranto observations (Vetrano et al., 1999; Cushman-Roisin et al., 2001).

The sea surface elevation fields at the open boundaries η_N and η_S can then be calculated from V_N and V_S using geostrophy and setting the sea surface elevation in the middle of each boundary to zero. The values η_N, V_N, η_S and V_S are used at the northern and southern boundaries respectively to specify
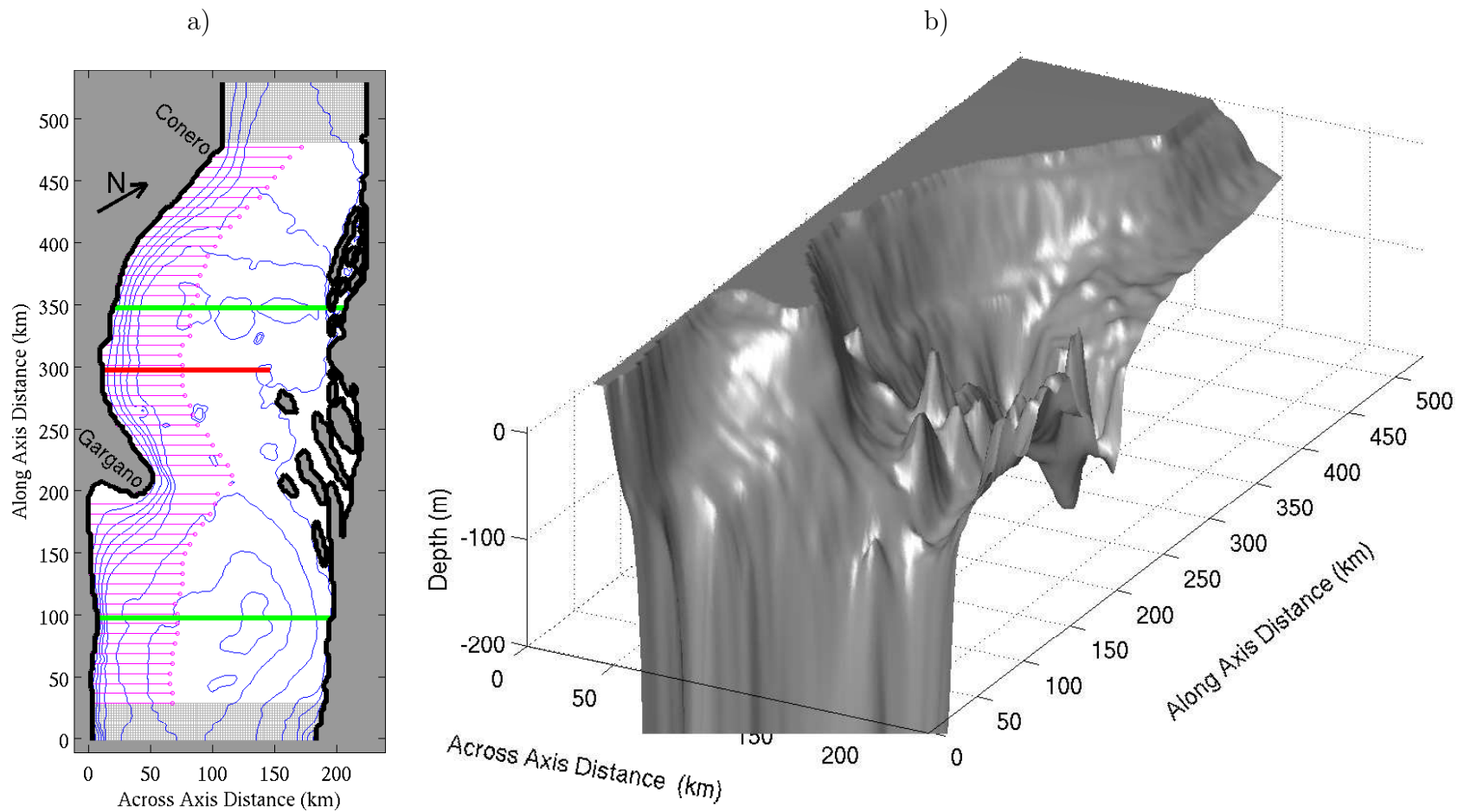
Fig. 4. a) Plan view of the numerical domain with axes oriented along and across the axis of the Adriatic Sea. The isobaths of 20 m, 40 m, 60 m, 80 m, 100 m, 200 m, 1000 m and 1200 m are shown; relaxation areas are shaded in gray. Sections functional to later calculations and discussions are also shown: in red the position of the zonal section for Fig. 7; the volume enclosed in the green zonal sections is used in Section 3.4; the magenta across-axis sections are used for the calculation of the baroclinic conversion term in Section 3.2 (every fourth section is shown in the picture). b) Three-dimensional close up of bathymetry around the Gargano Promontory.

13

Exp.	Wind direction	Wind speed	Δx	Days
Base	-	-	2 km	150
N	-	-	2 km	15
M	Northwesterly (downwelling)	7 m sec^{-1}	2 km	15
S	Southeasterly (upwelling)	7 m sec^{-1}	2 km	15
R	Realistic	Realistic	2 km	41
M-high	Northwesterly (downwelling)	7 m sec^{-1}	0.5 km	15
S-high	Southeasterly (upwelling)	7 m sec^{-1}	0.5 km	15
R-high	Realistic	Realistic	0.5 km	41

Table 2
The list of numerical experiments for this study.

the incoming characteristics via Flather conditions (Flather, 1976). Radiation conditions are applied at the open boundaries for the sea surface elevation, the baroclinic velocities and the tracers. In the south, the tracers are relaxed back to their initial values in an area 30 km long.

The final state of the base simulation is used as initial condition for all the subsequent runs. Three idealized experiments are set up. In the experiment N the flow evolves in absence of winds for another fifteen days. Two other experiments, denoted M and S, are run with downwelling Mistral and upwelling Sirocco winds. In both cases, wind speed is held at a constant value of 7 m sec^{-1} for fifteen days. This value represents an appropriate average for the period considered (see Table 1). Realistic wind data from the ALADIN atmospheric model are then used for another experiment (R) spanning forty-one days and covering the whole DART06b period. The ALADIN data are averaged over six hours on the 2-km horizontal grid.

Since implicit viscosity is used in these runs, the amount of numerical dissipation is a function of grid resolution. In order to explore whether different results are obtained by decreasing the horizontal mesh size, the last three experiments forced with wind are also run at higher resolution on a 0.5 km grid (M-high, S-high and R-high). Both model topography and coastline for the 0.5 km runs are interpolated from the 2 km grid. Since no topographic finer scales are introduced, the dynamical differences at the two resolutions are expected to be mainly dependent on the inherent different effective numerical viscosity used in the runs.

The simulations are run with different timesteps always respecting the CFL condition and their computational times vary. In the case of the fortyone day high resolution realistic experiment (R-high), the baroclinic and barotropic timesteps are $\Delta t_i = 25.0$ sec and $\Delta t_e = 0.833$ sec, respectively. The model cycles for $141,696$ baroclinic iterations and the simulation requires a wall-clock time of about four days using sixtyfour processors on an IBM $\mathrm{p5} - 575$ cluster. Table 2 summarizes the different experiments considered in this study.

3   Results

3.1   Baseline experiment

Fig. 5 shows the evolution of the surface salinity field in the baseline experiment. The evolution of a steady coastal current along a straight coast in absence of wind has already been described (e.g. Yankovsky and Chapman, 1997; Lentz and Helfrich, 2002). For plumes in contact with the seafloor, an important role is played by bottom friction (Chapman and Lentz, 1994). The bottom Ekman layer forces the foot of the plume to move offshore until an equilibrium is reached. At that point the bottom geostrophic flow at the front is zero and the plume stops spreading offshore. A similar evolution can be found in the simulation. Since the coastal current is buoyancy driven, it flows along the Italian coast being deflected to the right by the Coriolis force. During its path, however, it runs first into the reentrance downstream of the Conero and then into the Gargano Promontory. Such a complex coastline forces the fluid to temporarily separate from the coast and instabilities are created. Eddies are especially evident around the Gargano Promontory. In its lee, two small vortices form, which are eventually replaced by a large lee anticyclone. Its horizontal dimension is similar to the across-shore length of the Promontory, and its formation can be therefore attributed to the process of separation behind an obstacle (Batchelor, 1967; Schlichting and Gersten, 2003).

The offshore edge of the current is characterized by different instabilities. Small eddies, squirts and mushroom-like structures can be found in the panels of Fig. 5. The fresher water intrusion is larger in the northern part of the domain but it remains confined in the south due to potential vorticity barriers created by the geomorphology of the basin. Riverine waters have easy access to the northern offshore portion of the domain, where the shelf is gentler and the Adriatic bathymetry shoals. In the middle, the coastal current tends to be confined onshore for the presence of the steeper and well-defined shelf. Further south, downstream of the Gargano Promontory, the presence of the South Adriatic Pit forces the waters to remain onshore as they approach and exit the numerical domain.
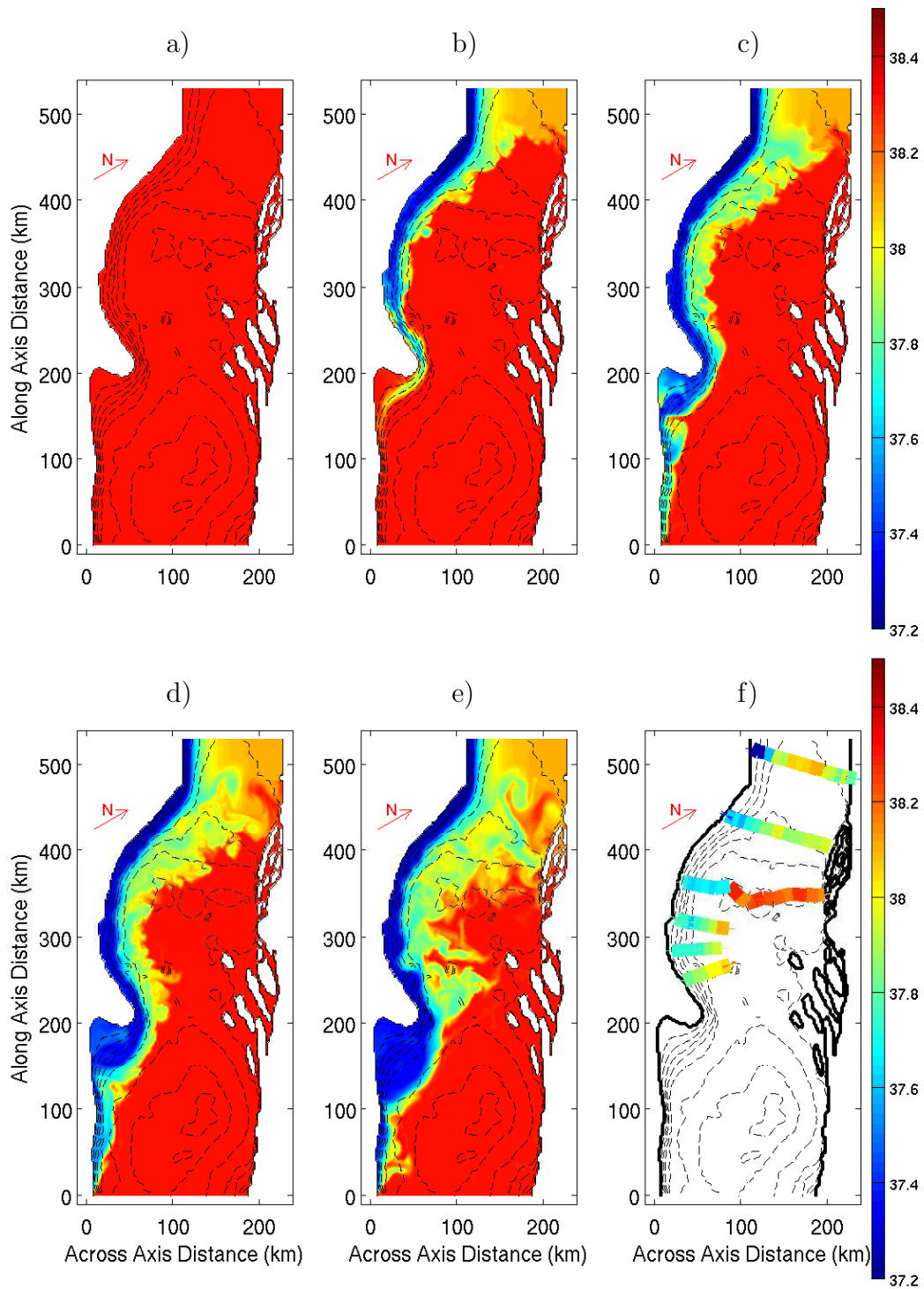
Fig. 5. Model surface salinity field: a) Initial and after b) 1 month; c) 2 months;
d) 3 months; e) 5 months. f) Surface salinity data collected during August 16-18,
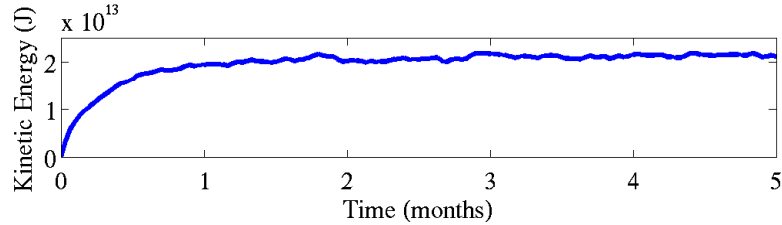2006. Dashed lines indicate same isobaths as in Fig. 4.

Fig. 6. Total kinetic energy versus time for the baseline experiment.

Fig. 5 shows that after two months of initial adjustment, the simulation can be considered in equilibrium. Details may evolve but the general pattern remains the same. This is confirmed by the total kinetic energy plot in time (Fig. 6) where after two months a plateau is reached. Panel f) of Fig. 5 shows the surface salinity data collected during DART06b by the Research Vessel Dallaporta. Data are compared with the results of the simulation after five months (Fig. 5e). The aim is a process study and the interest is to see whether the obtained fields can be considered realistic and in qualitative agreement with observations. A precise match is not to be expected since the simulation is just boundary and buoyancy driven, and it does not consider all the other forcings used in operational models. Nevertheless, the salinity field after five months of idealized simulation is in qualitative agreement with the data. Particularly important is the position of the offshore saltier ambient (red) water. Data show that this water sits on the Middle Adriatic Pit. The simulation is able to reproduce this front. Its position is stable once the initial adjustment time has passed. The front looks sharper in the actual data, but the plume is saltier. It is speculated that is mainly due to the lack of additional mixing due to wind forcing (see section 3.4).

3.2   Idealized experiments: no wind, Mistral and Sirocco

The salinity field of Fig. 5e is used to initialize each of the experiments under idealized wind conditions lasting fifteen days. Fig. 7 compares zonal sections of the salinity fields after one week in the three cases. The location of the (red) section is shown in Fig. 4a.

Without wind (Fig. 7a), the plume exhibits a typical wedge shape whose thickness gradually decreases offshore. The current core stays offshore while the area onshore remains relatively quiescent as described in the literature (e.g. Lentz and Helfrich, 2002). Northwesterly Mistral winds are downwelling favorable for the Italian coast. As a result, the coastal current is stronger and its core is closer to the coast (Fig. 7b). Its across-shore width decreases while its thickness increases for mass conservation. Since the front steepens, the contact between riverine and saltier waters reduces in area. Furthermore,

17

a) No wind

b) Downwelling Mistral winds

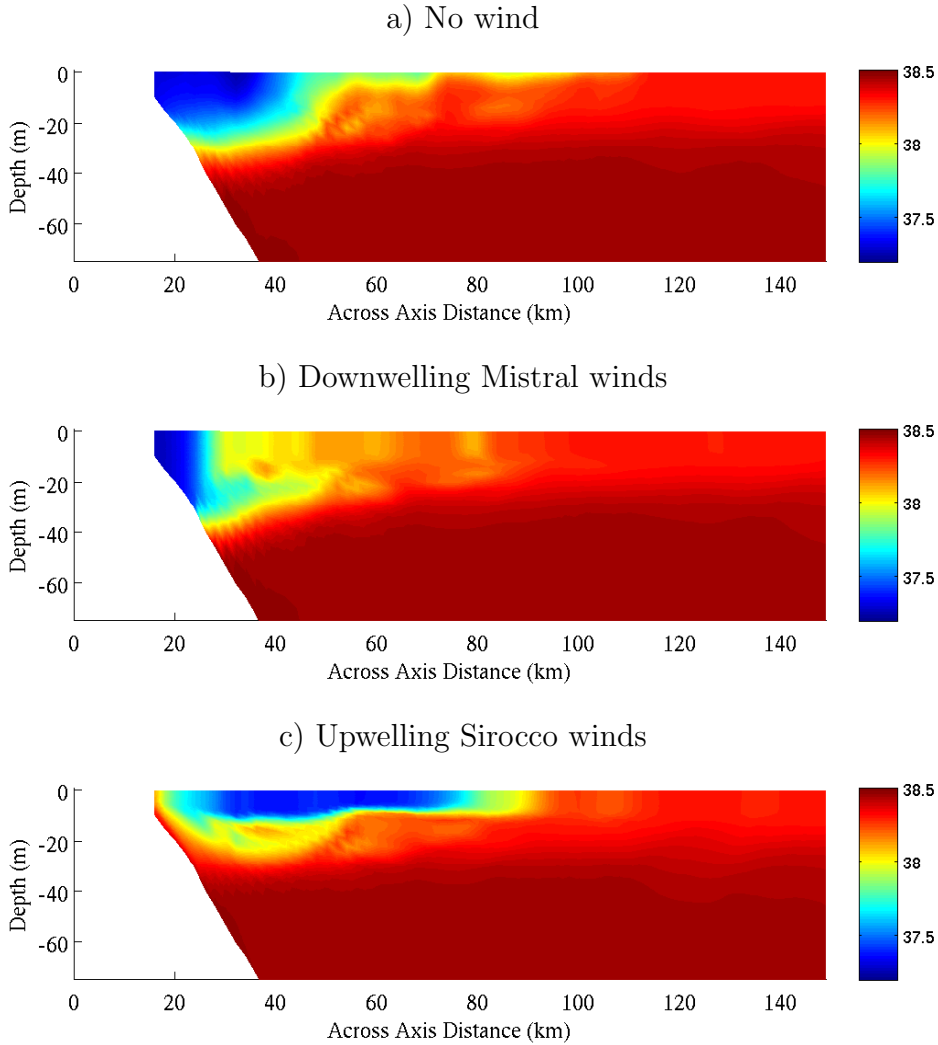### c) Upwelling Sirocco winds

Fig. 7. Zonal sections of the salinity field after one week of the idealized fifteen days experiments. a) No Wind; b) Mistral and c) Sirocco winds. Note that the vertical terrain-following grid gets stretched near the boundary and color interpolation follows its edges.

since the coastal current width decreases, the plume surface where the wind stress can act reduces as well. In these conditions, mixing mainly happens at the plume base where vertical shear is maximum. Here some fresh waters mix with the saltier ones below and create intermediate waters which equilibrate at depth. The result is a lenticular feature almost detaching from the coast and extending at intermediate depth offshore. Since mixing is so localized, the coastal current remains relatively fresh. This statement will be quantified later in section 3.4 of the paper.

Southeasterly Sirocco winds are upwelling favorable for the Italian coast. The coastal current is pushed offshore while its thickness reduces and its width

18
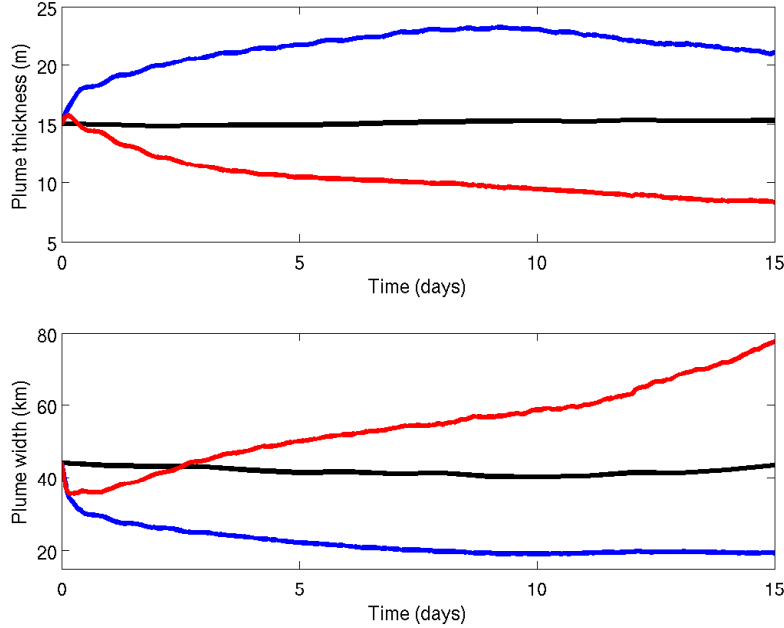
Fig. 8. Average plume thickness and width for the idealized wind experiments: no wind (black line), Mistral (blue line) and Sirocco (red line).

increases (Fig. 7c). The current also reverses direction. Mixing occurs initially at the offshore plume edge due to the gradual decrease of the thickness and according to the mechanisms described by Fong and Geyer (2001). Additional lateral mixing happens onshore after the detachment of the plume. Mixing is also enhanced since the surface of contact between fresher and saltier waters increases in area as the front flattens. Since the plume is wider, winds can also act on a larger plume surface. As a result, contrary to the above situation, upwelling winds can cancel most of the plume freshwater signal. As stated previously, this important difference is better analyzed later in section 3.4.

The differences in the three cases can be quantified with the averaged plume thicknesses and widths in the domain (Fig. 8). These quantities are calculated based on the averaged maximum section depths and offshore extensions at which plume waters can be found. Plume waters have salinity $S \leq 38$ and relaxation areas are excluded from the averages. In the absence of wind (Fig. 8, black lines) the plume has an average thickness of about 15 m. The coastal current tends to be 42 km wide and this width remains almost constant in time. Under downwelling conditions, its averaged across-shore width halves while its thickness increases and settles above 20 m (Fig. 8, blue lines). With upwelling winds, the averaged thickness keeps reducing while the width increases (Fig. 8, red lines). The rapid initial decrease (increase) in width (thickness) is explained by the fact that the plume initially mixes at its outer edge more rapidly than being advected offshore. This is another clear indication of the strong lateral mixing happening when Sirocco winds blow.

a) No wind
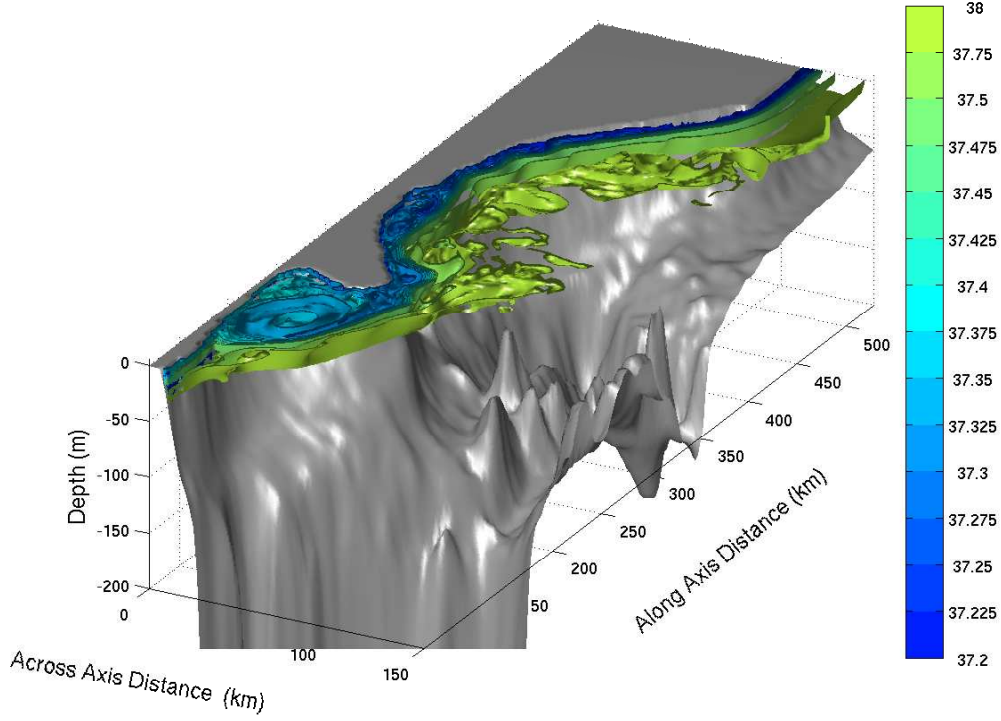
b) Downwelling Mistral winds
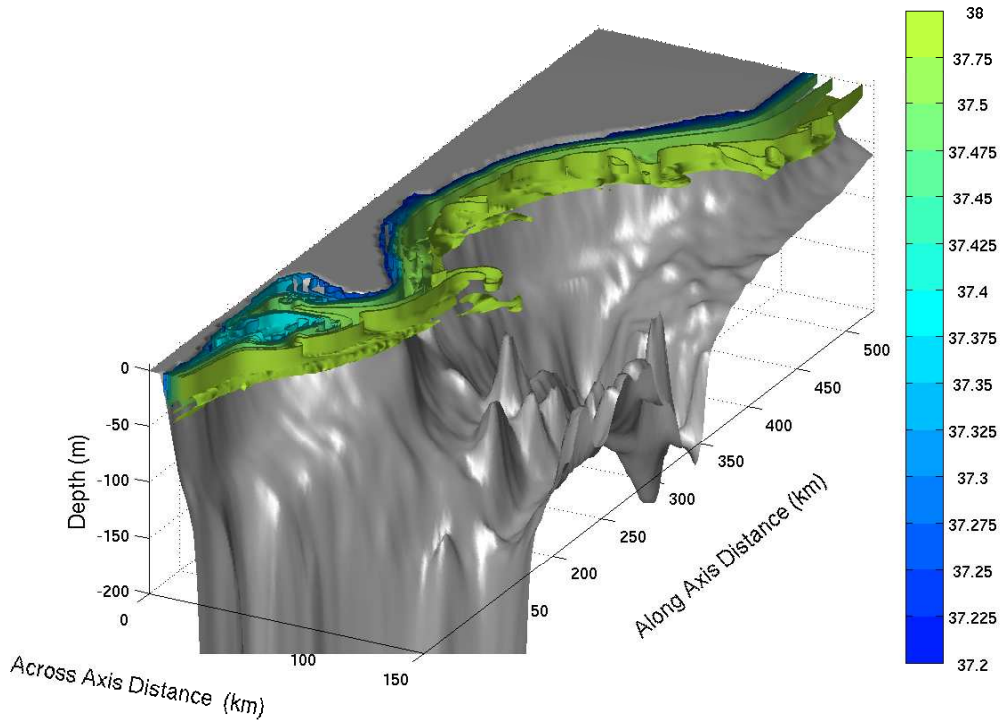
Fig. 9. Three-dimensional close up of salinity isosurfaces after one week of the idealized fifteen days experiments. Note that the colorbar is not linear. a) No Wind; b) Mistral and c) Sirocco.

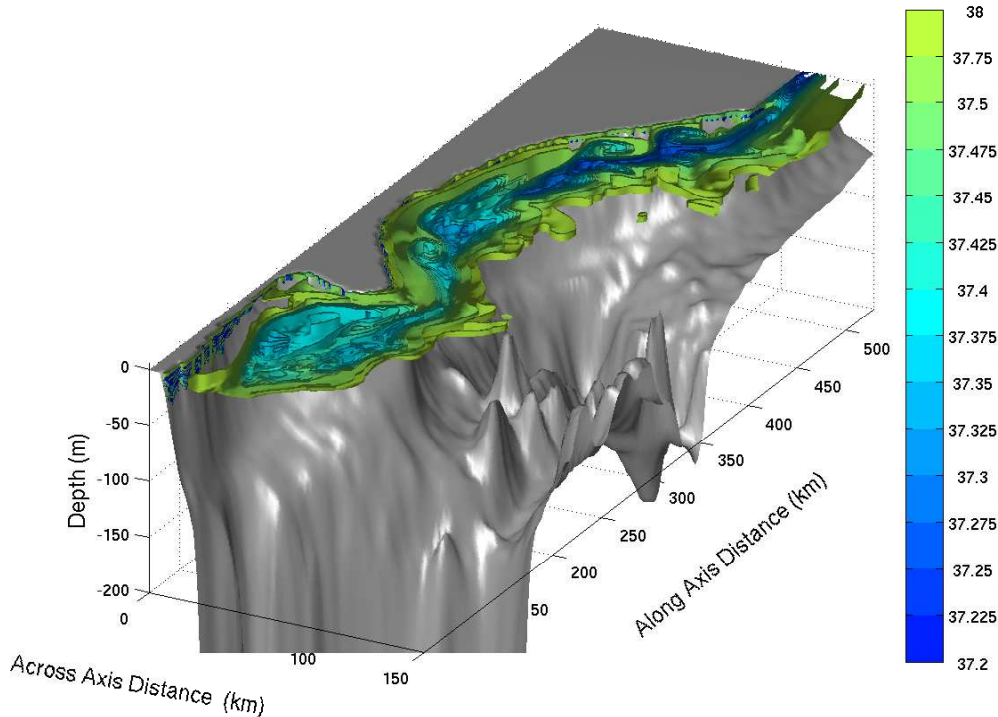c) Upwelling Sirocco winds

Fig. 9. continued.

Three-dimensional salinity isosurfaces can be used for a first qualitative assessment of the turbulent state of the coastal current in the three cases (Fig. 9). The fields are presented after one week of simulation as in Fig. 7. In the absence of wind (Fig. 9a), different eddies are observed onshore and upstream of Gargano Promontory, while a larger anticyclone can be found in its lee. Filaments, squirts and smaller instabilities are present at the outer edge of the current. In downwelling conditions (Fig. 9b), the coastal current appears more steady and the anticyclone in the lee of Gargano Promontory is weaker. The picture shows well that the lenticular feature of Fig. 7b is common to the whole domain. With upwelling winds (Fig. 9c) filaments and turbulent structures develop on the border of the coastal current.

A more quantitative comparison between the idealized experiments with Mistral and Sirocco winds can be obtained by calculating the baroclinic conversion term C_{blc}. The term is defined as $C_{blc} = -g\rho'w'$, where ρ' and w' are the deviations of density ρ, and vertical current velocity w, from the fifteen-day averaged fields in each point of the domain. The density ρ is calculated from the model temperature and salinity fields via a nonlinear equation of state (Jackett and McDougall, 1995). A positive C_{blc} implies conversion of potential energy to eddy kinetic energy via baroclinic instabilities (Harrison and Robinson, 1978). In this respect, the baroclinic conversion term is only used

21
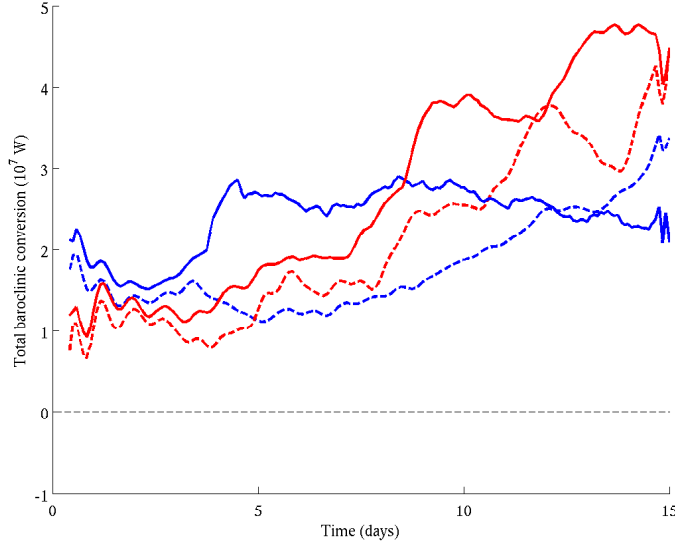
Fig. 10. Evolution of C_{blc}^{tot} for the idealized experiments. Dashed lines stands for the 2 km simulations, solid lines for the 0.5 km ones. Blue color for Mistral, red for Sirocco.

as a quantitative measure of the differences among the runs forced by different idealized winds.

In the following, the temporal conversion variability is investigated by calculating the volume integrated baroclinic term $C_{blc}^{tot}(t) = -\int g\rho'w'\,dV$. Since the interest is on the WAC dynamics, only points offshore the Italian coast are considered in the calculation of C_{blc}^{tot} (see magenta offshore sections in Fig. 4a). Results for the two different resolutions are also compared (Fig. 10). Furthermore, plan views of the surface C_{blc} patterns provide important information about the nature of the instabilities in the different cases (Fig. 11, 12 and 13).

The baroclinic instability mechanism remains active in all idealized wind simulations since C_{blc}^{tot} is positive at all times (Fig. 10), even though C_{blc} values may be large negative in certain parts of the model domain (see Fig. 11 and 12). As expected, the higher resolution results generally in larger values since numerical dissipation is a function of grid spacing and finer instabilities can emerge when it is reduced.

In the first week of the 2 km Mistral simulation (Fig. 10, blue-dashed line), the turbulent state remains somewhat similar to the initial moments. Afterwards C_{blc}^{tot} starts increasing and narrow positive surface C_{blc} areas, confined to the WAC borders, start to appear (Fig. 11a and b). Four days later, wave-like irregularities are found within the coastal current around Gargano Promontory (Fig. 11d). Their dimension is about 10 km; a little bit larger than the estimate for the deformation radius ($\simeq 7$ km). The instabilities are observed to break backward relative to the direction of the current (Fig. 11e) and be associated
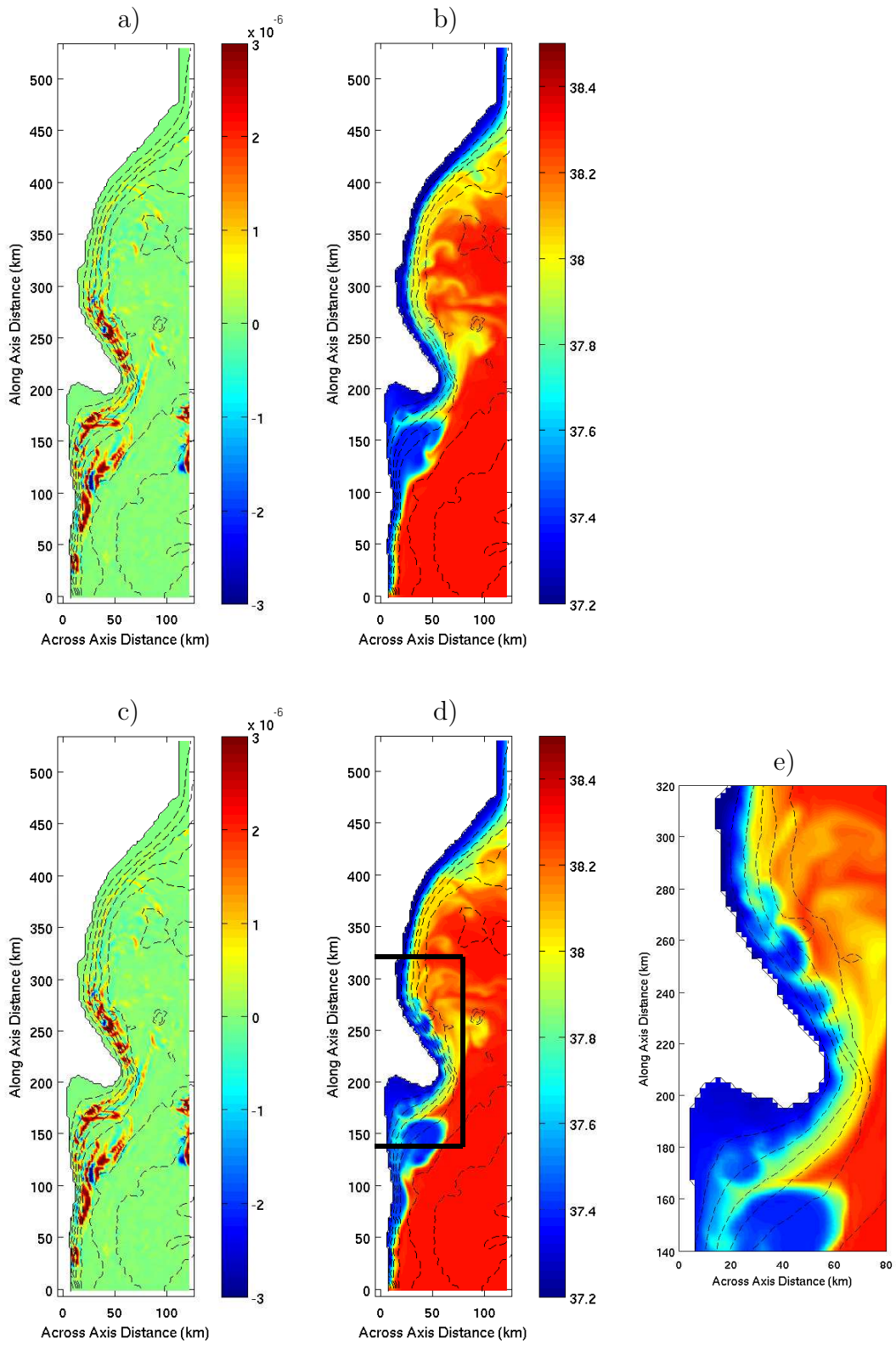
22

Fig. 11. Surface fields for the 2 km idealized experiment with Mistral winds. a) C_{blc} (W m^{-3}) and b) salinity after 7 days; c) C_{blc} (W m^{-3}) and d) salinity after 11 days. e) Close up of salinity after 11 days for the area enclosed in the box in d).
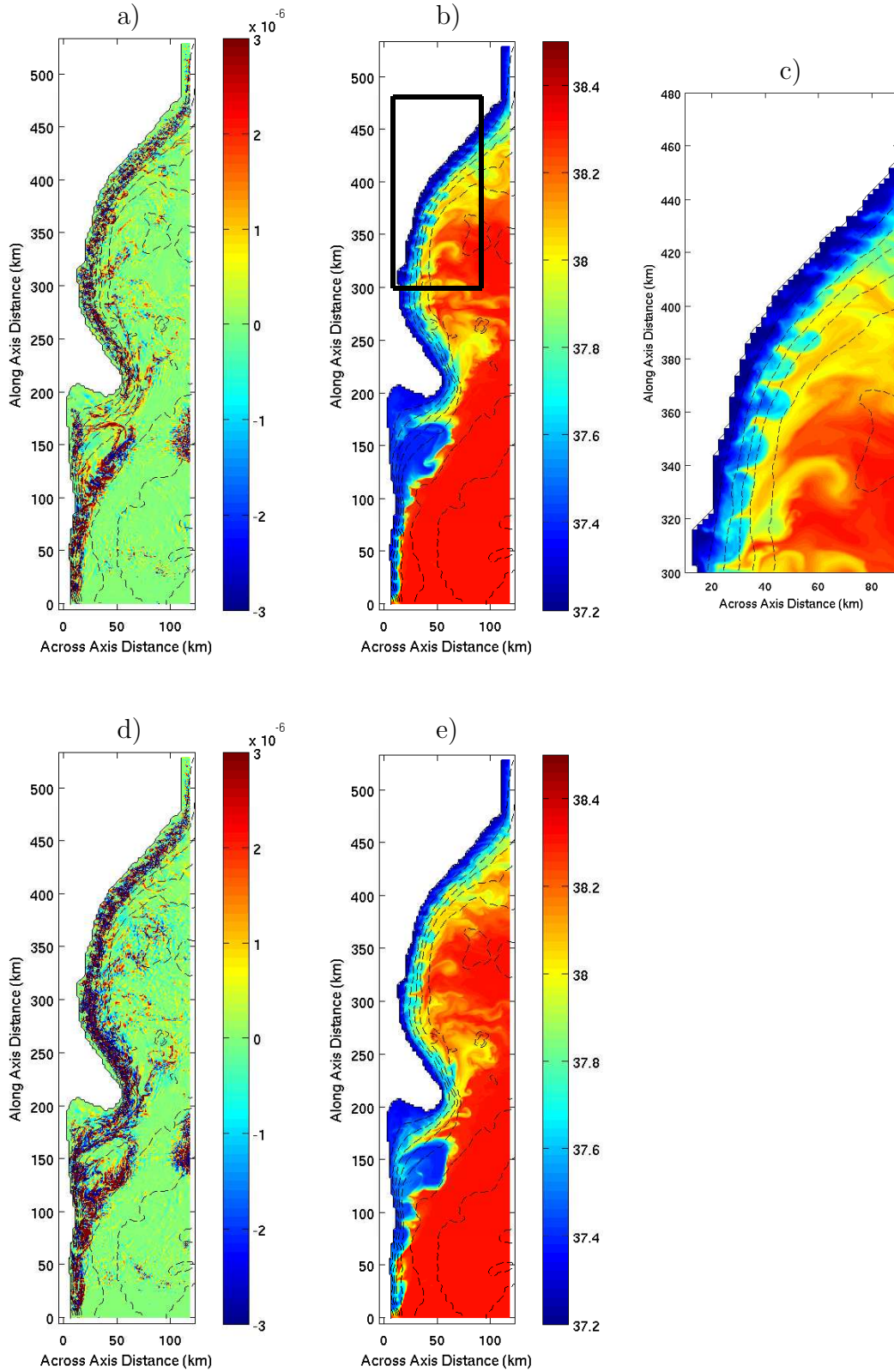
23

Fig. 12. Surface fields for the 500 m idealized experiment with Mistral winds. a) C_{blc} (W m^{-3}) and b) salinity after 7 days. c) Close up of salinity after 7 days for the area enclosed in the box in b). d) C_{blc} (W m^{-3}) and e) salinity after 11 days.
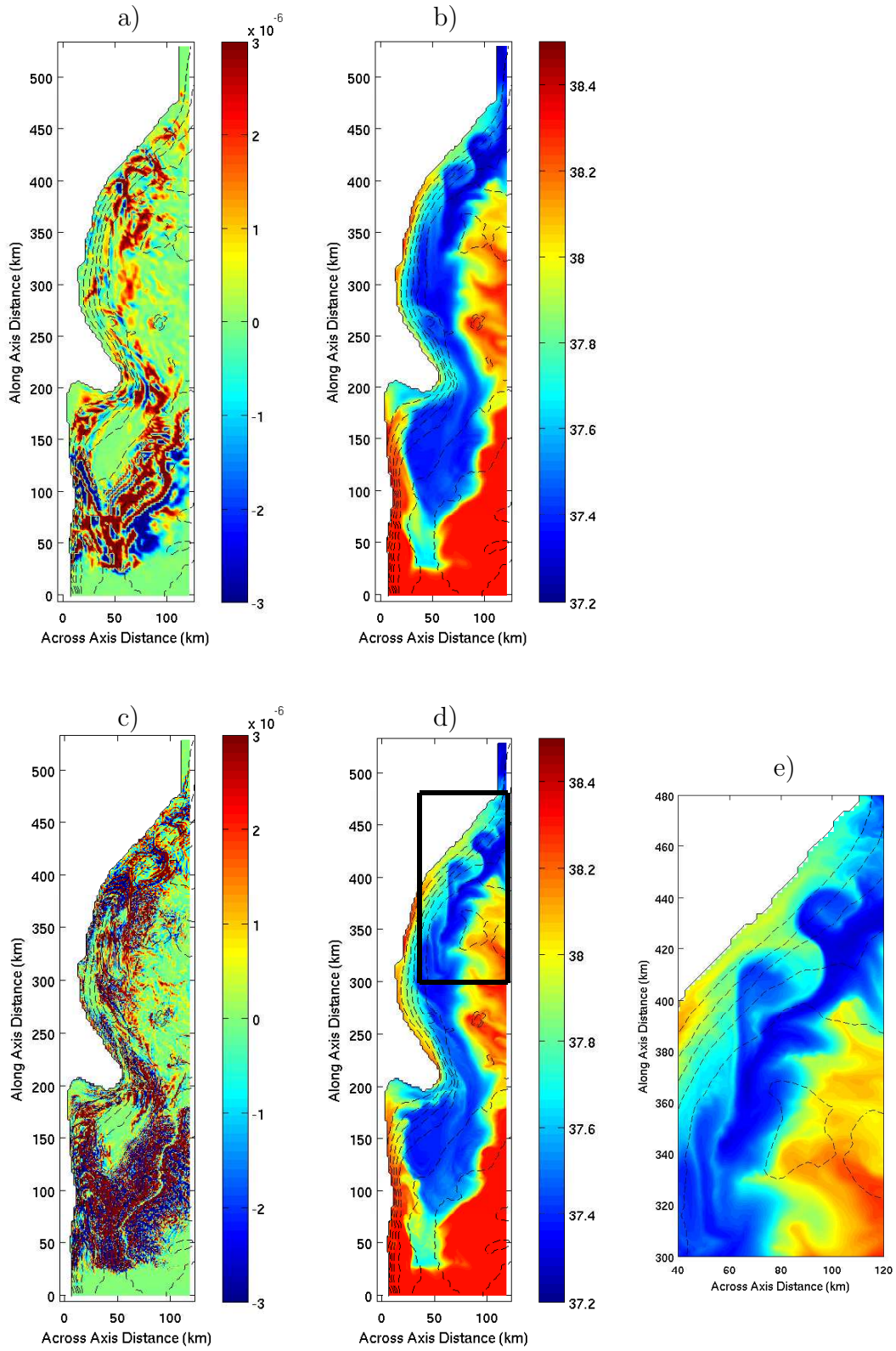
Fig. 13. Surface fields after 7 days for the idealized experiments with Sirocco winds. a) C_{blc} (W m^{-3}) for $\Delta x = 2$ km and b) salinity for $\Delta x = 2$ km. c) C_{blc} (W m^{-3}) for $\Delta x = 0.5$ km and d) salinity for $\Delta x = 0.5$ km. e) Close up of salinity for $\Delta x = 0.5$ km for the area enclosed in the box in d).

with higher positive C_{blc} values (Fig. 11c). Their formation is known in the literature and seems to be associated with the cascade of denser water pushed onshore by the downwelling winds via Ekman dynamics (Thomas and Lee, 2005). Wave-like irregularities persist almost for the whole simulation, fading away in the very last hours of the fifteen-day simulation.

At 0.5 km resolution, C_{blc}^{tot} already increases in the first week of simulation (Fig. 10, blue-solid line) since an earlier onset of these structures is observed. After seven days, the whole WAC is already corrugated by wave-like features and positive C_{blc} areas are found all along the Italian coast (Fig. 12a and b). In the northern part of the domain, other instabilities seem to be the precursor for the backward breaking structures (Fig. 12c). Having an earlier onset, these structures also tend to vanish earlier: four days later, few wave-like irregularities are found within the coastal current (Fig. 12e) since the WAC narrows and the instabilities do not have enough across-shore room to develop and grow. In the surface C_{blc} fields, more negative areas appear (Fig. 12d). Fig. 10 shows that C_{blc}^{tot} starts decreasing after ten days, ultimately reaching a lower value than in the coarse resolution.

For the 2 km Sirocco simulation, the turbulent increase happens after about five days (Fig. 10, red-dashed line). As soon as baroclinic disturbances form, they have enough across-shore space to develop and grow to form mesoscale features. After one week their dimension is around three times the deformation radius. The two anticyclones forming downstream of Conero Promontory (Fig. 13b) recall closely the ones in the same area evident in Fig. 1a and simulated by Korotenko (2007). Note that the structures behind the Conero Promontory are also simulated in some of the experiments by Cushman-Roisin et al. (2007), where either the coastline is straightened or the topography altered (all depths less than 100 m are deepened to 100 m). This confirms that the main mechanism for their formation is baroclinic instability while both coastline curvature and bottom topography may play secondary roles. Larger positive C_{blc} areas are found at the border of these features as well as in the other frontal regions (Fig. 13a). In the last part of the simulation, mesoscale eddies keep growing, reaching and then stabilizing at a dimension of about 35 km (not shown). This dimension is realistic and observed elsewhere (Cushman-Roisin et al., 2007). For both resolutions with Sirocco winds, C_{blc}^{tot} rapidly increases reaching higher values than with Mistral winds. The 0.5 km resolution fields just show the same structures observed at 2 km with better detail (Fig. 13c, d and e).
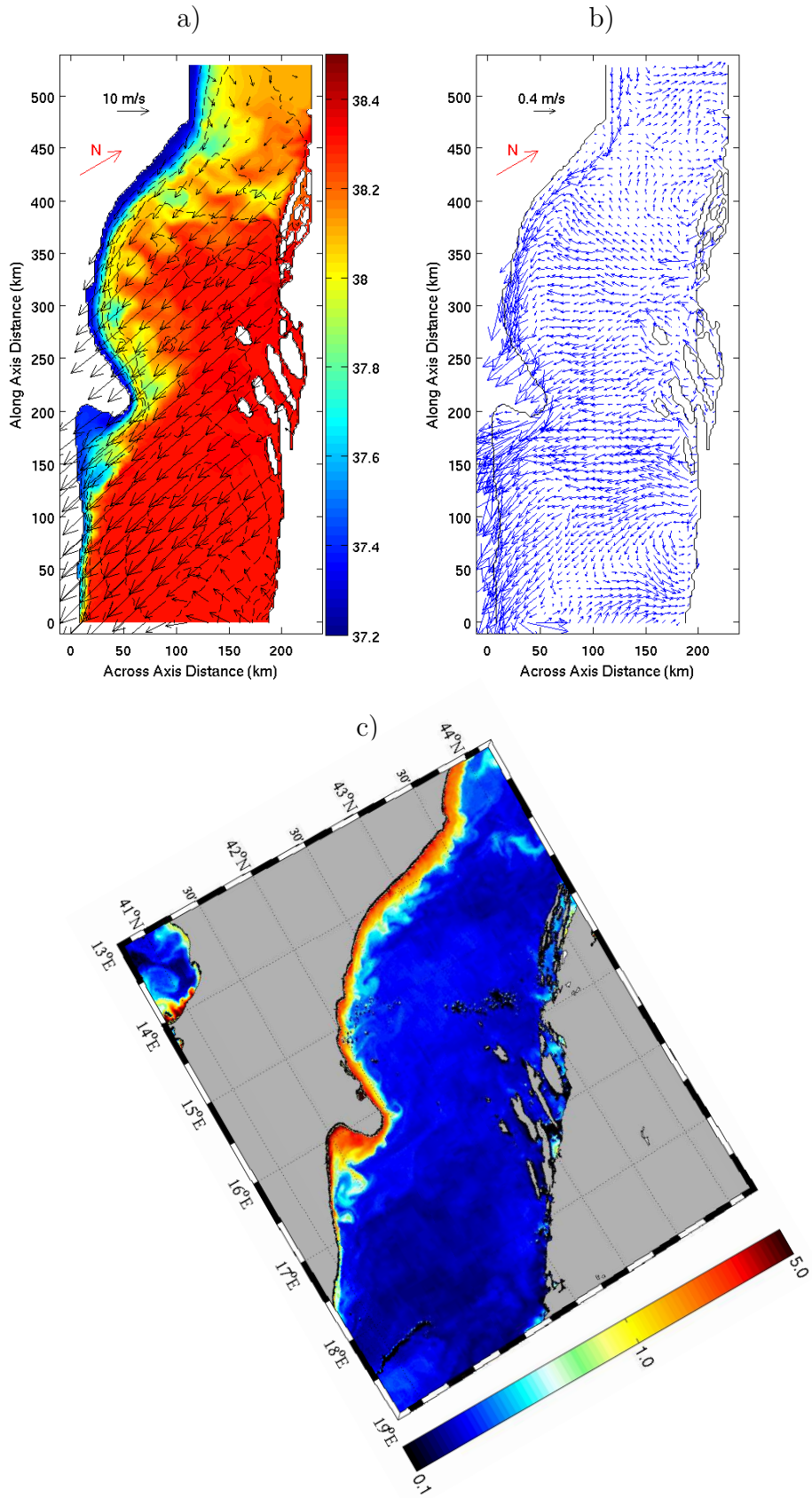
Fig. 14. August 31: a) Winds and simulated surface salinity; b) Simulated surface velocity; c) Chl-A Modis (mg m^{-3}) image for the same day processed by SeaDAS.
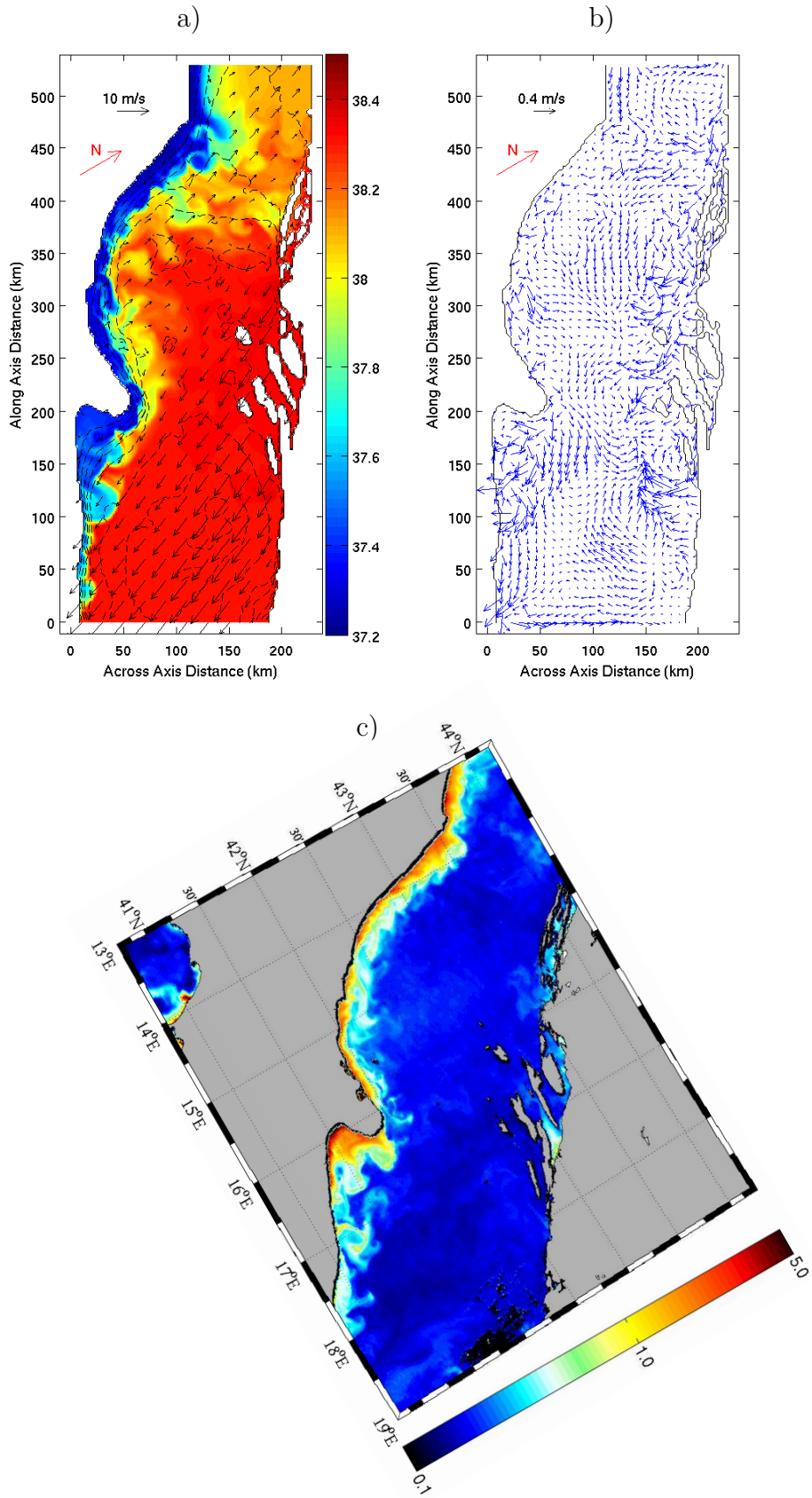
a)
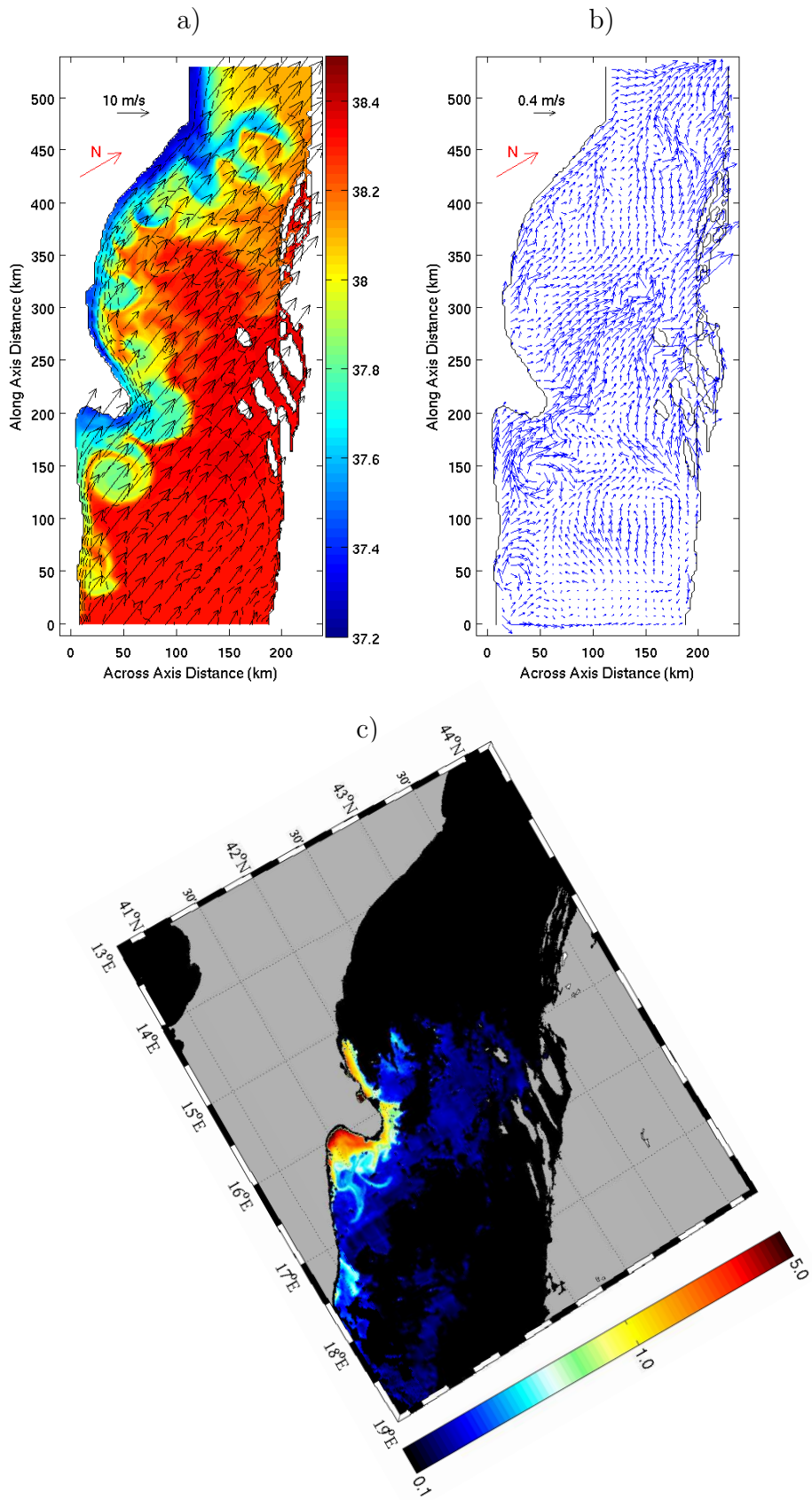
b)

c)

Fig. 15. As in Fig. 14 but for September 4.

Fig. 16. As in Fig. 14 but for September 14.

The surface salinity field after five months of the baseline experiment is also used as an initial condition for a simulation forced by realistic wind and spanning the whole DART06b period. In the last two weeks of August 2006 the wind pattern is not organized or spatially coherent. The intensity of the winds remains also low and the general salinity distribution is almost the same as in Fig. 5e.

The situation changes dramatically when, on August 30, the strong Mistral event starts. Fig. 14 shows the situation after one day. As in the idealized Mistral simulation, the WAC narrows and accelerates, the salinity front moves onshore and the currents appear more steady since the number of larger instabilities decreases. The Chlorophyll-A satellite image taken at the same time shows a qualitatively similar situation: a narrow and smooth WAC with few corrugations. Low salinity waters (37.2) in the simulation are still present onshore in a narrow strip along the whole Italian coast.

The strong Mistral event is followed by a period of relaxation of wind intensity. Since winds relax, the system moves toward a state as in the absence of wind. This state is characterized by a coastal current tending to spread offshore and fragmented by instabilities. On September 4, i.e. after three days of relative calm, the WAC is indeed wider and corrugated by larger turbulent features all around the Italian coast (see Fig. 15). In the following days, weak local winds affect the evolution and growth of the turbulent structures. In the lee of Gargano Promontory, the weak winds pulsate, often reversing their direction. This is probably due to the orography of the same Promontory and to its shadow effect (Pasarić et al., 2009).

In the following days, different smaller structures merge in two larger eddies which experience strong modifications when strong Sirocco winds start to blow on September 13. Fig. 16 shows the situation after only one day of Sirocco winds. The whole WAC and all the instabilities are soon pushed offshore. Squirts and jets are noticeable in the northern part of the domain while, upstream of Gargano Promontory, two mushroom-like features extend offshore. Under these conditions, fresh waters apparently experience strong lateral mixing off and onshore, and the initial fresh water signal fades away. The two larger instabilities are in fact characterized by waters 0.5 saltier than 10 days before. The satellite image in this day is broken by clouds and less clear than the previous ones. In the subsequent days, when strong Sirocco winds keep blowing, mixing is further enhanced and the WAC is pushed more offshore. The two eddies eventually merge, forming a large area of intermediate salinity (37.8) in the lee of Gargano Promontory (not shown).
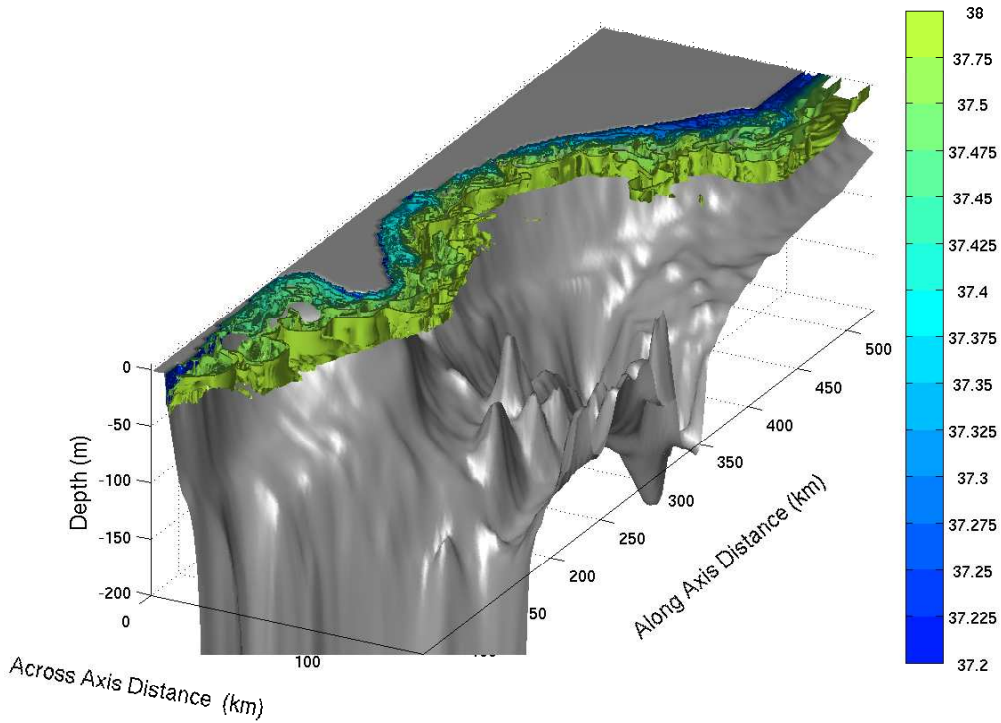
a) 2 km Resolution
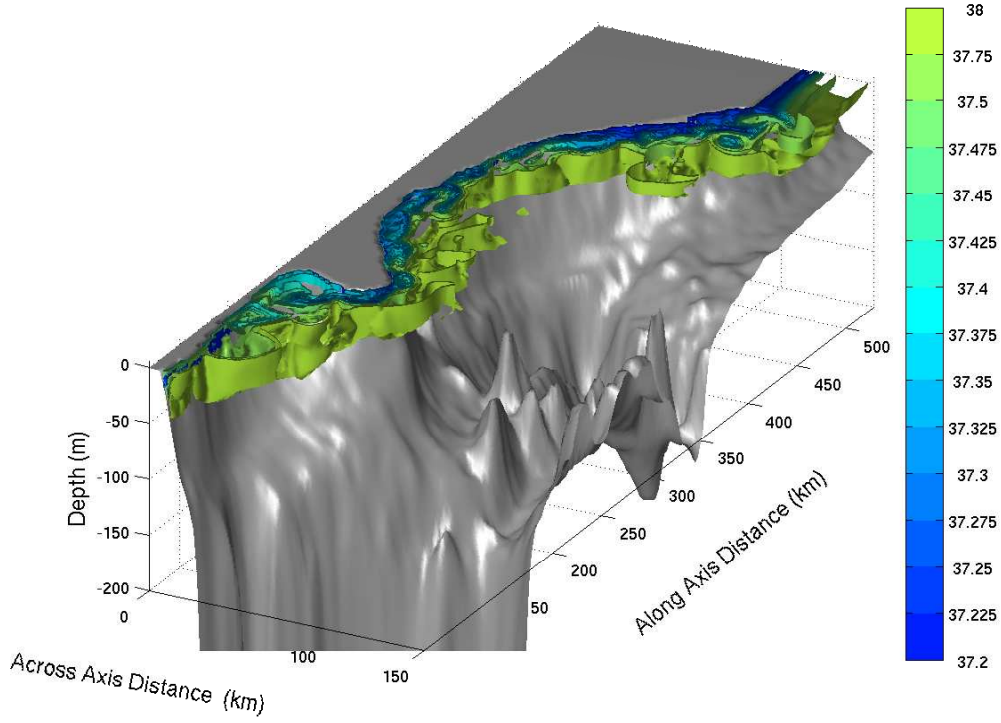
b) 0.5 km Resolution

Fig. 17. Comparison of salinity isosurfaces for September 4 in the low and high resolution realistic runs. Note that the colorbar is not linear. a) 2 km and b) 0.5 km .

The simulation run on the 0.5 km grid shows the same general trends of the low resolution case. However, as in the idealized experiments, the instability process can be observed in much more detail especially when turbulent features are enhanced. Fig. 17 shows a three-dimensional comparison between the low and high resolution simulations forced by realistic winds. Finer turbulent structures are observed in the whole domain when the mesh of the grid decreases. The coastal current also experiences more mixing in the 0.5 km run since saltier waters are found along the Italian coast. This difference is better quantified in the next section.

3.4   Mixing

The figures of the previous section suggest different types of transformation of the water masses under various wind conditions. To quantify these differences, the total volume enclosed by the two green zonal sections shown in Fig. 4a is considered. Four different salinity classes are chosen and the volumes for each class calculated. Plume waters are split into two subclasses, $S \leq 37.5$ and $37.5 < S \leq 38.0$. Intermediate waters are in the class $38.0 < S < 38.3$, while the initial ambient waters are all included in the saltiest class $S \geq 38.3$. The calculation is restricted to the first 100 m in depth, since only water belonging to the saltiest class crosses this surface.

Fig. 18a shows the initial state common to all these experiments. The subsequent panels show the net volume gain or loss at two different times in different idealized wind conditions. When the simulation is run without wind forcing, not much happens in terms of water transformation (Fig. 18b and c). With Mistral winds, some of the freshest water is forced to mix and its volume decreases in time (Fig. 18d and e). The volume of the saltiest class decreases too. The net result is an increase of the waters within the intermediate classes $37.5 < S \leq 38.0$ and $38.0 < S < 38.3$. Even though part of the freshest water is lost, the class $37.5 < S \leq 38$ still increases, the total volume of water with salinity $S \leq 38$ remains close to the initial value and the coastal current maintains its freshwater signal. Under Sirocco conditions instead (Fig. 18f and g), a larger volume of water in the freshest class mixes and the volume of the class $37.5 < S \leq 38.0$ remains more or less the same. Therefore, contrary to what happens under Mistral conditions, the coastal current looses an important part of its freshwater signal. When resolution is increased, the same trends are observed (Fig. 19) and a larger decrease in the volume of the freshest class is achieved.

Since the focus of this study is on the Western Adriatic Current, it is useful to follow the evolution in time in the realistic runs of the net volume gain or loss for the $S \leq 38$ water, denoted as $\Delta \mathcal{V}_{S \leq 38}$. $\Delta \mathcal{V}_{S \leq 38}$ is expressed as volume
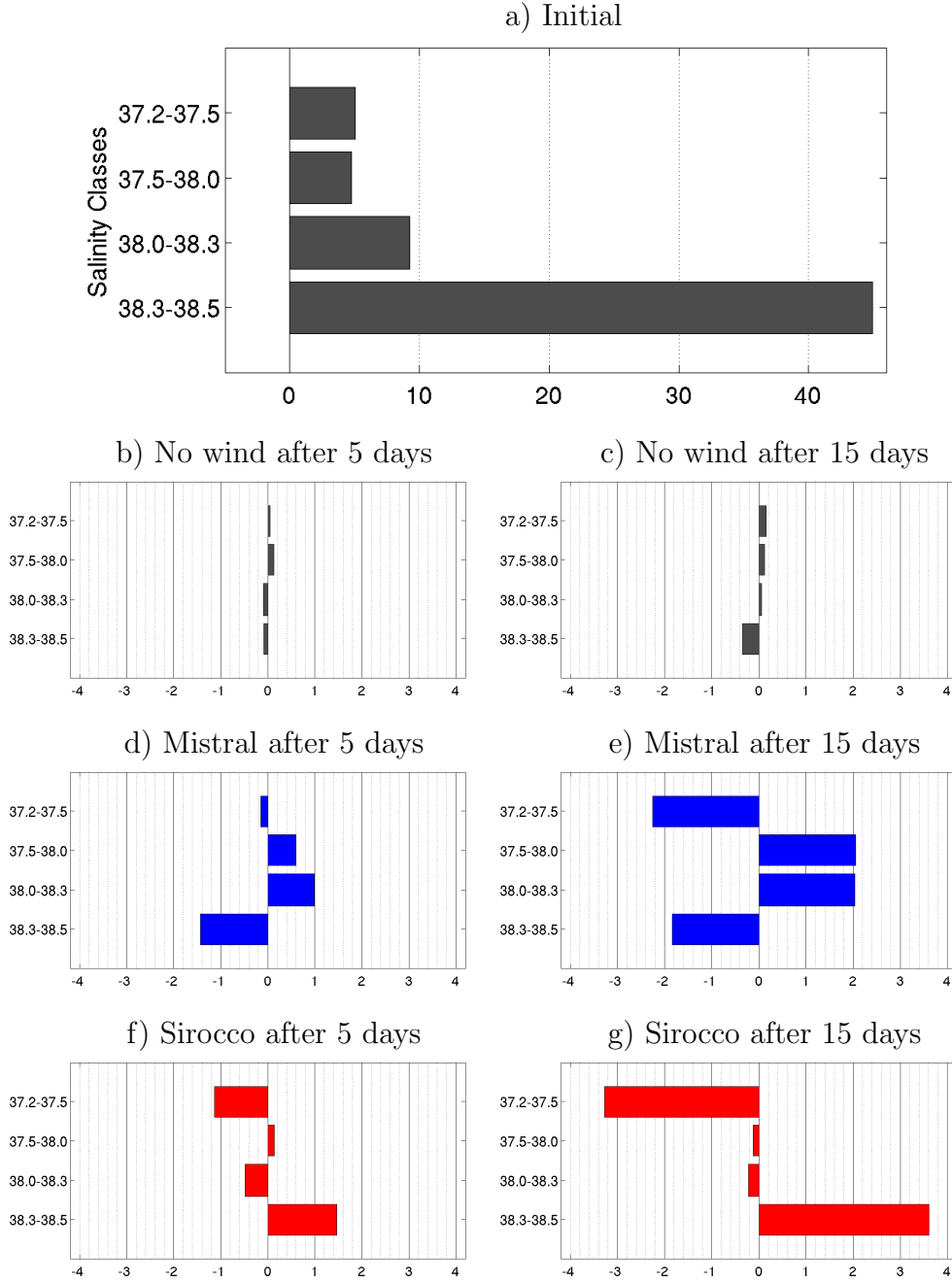
Fig. 18. Volumes for salinity classes in the 2 km idealized experiments. Top panel shows initial condition. Other panels show differences with respect to the initial condition. Units are 10^{21} m^3.

difference with respect to the initial state and considers the volumes of the first two classes together. In Fig. 20 the values of $\Delta\mathcal{V}_{S\leq 38}$ for the two different resolution (blue lines) are shown with the meridional component of the wind stress averaged on the whole domain (denoted as $<\tau_y^s>$, black line). Positive (negative) values of $<\tau_y^s>$ are indicative of upwelling (downwelling) favorable
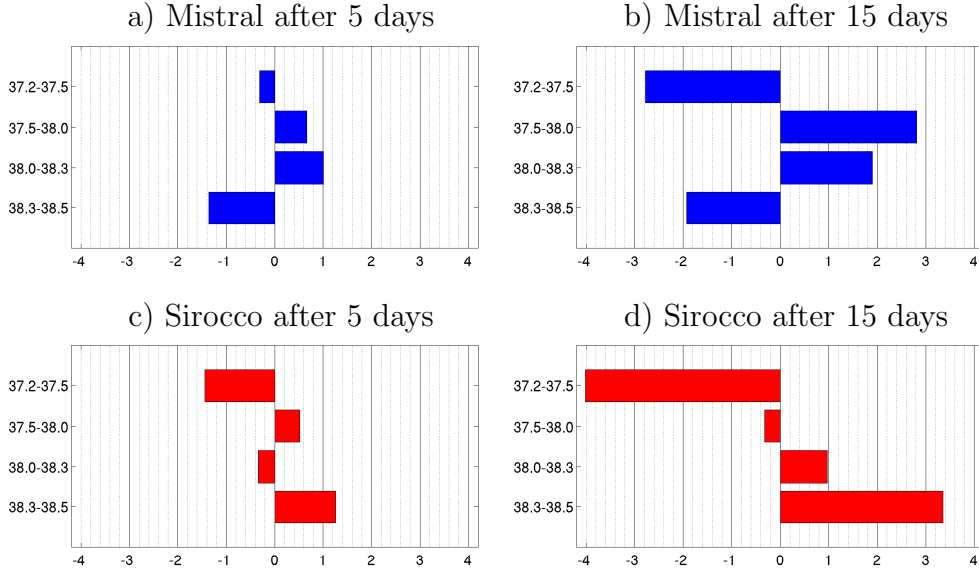
Fig. 19. Volumes differences with respect to the initial condition for salinity classes in the 0.5 km idealized experiments. Units are 10^{21} m^3.
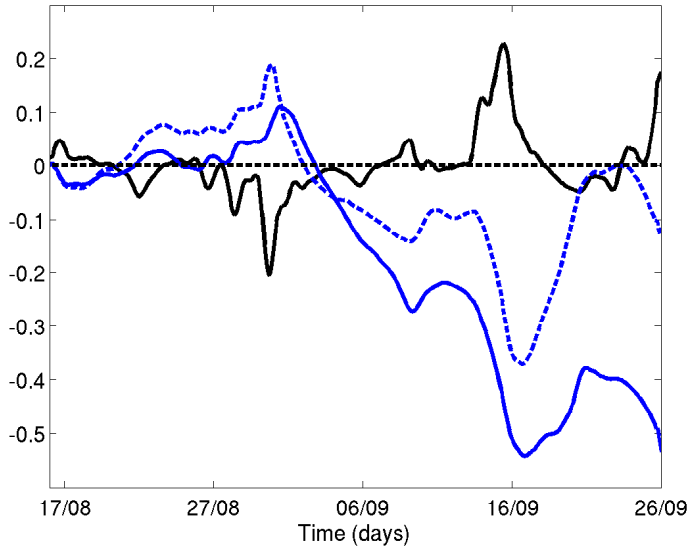

Fig. 20. Evolution of $\Delta \mathcal{V}_{S \leq 38}$ ($5 \cdot 10^{21}$ m^3, blue lines) and $<\tau_y^s>$ (Pa, black line) for the realistic experiment. Dashed blue line stands for the 2 km simulation, continued blue line for the 0.5 km one. Variables are defined in the text.

conditions. Note that the variable $<\tau_y^s>$ is a good indication for the sequence of events already shown in Fig. 3.2: a strong Mistral event starting on August 30 and the strong Sirocco event starting on September 13.

For both resolutions, as in the idealized Mistral experiments, the freshwater decrease is compensated by the creation of slightly denser fresh water. As a re-
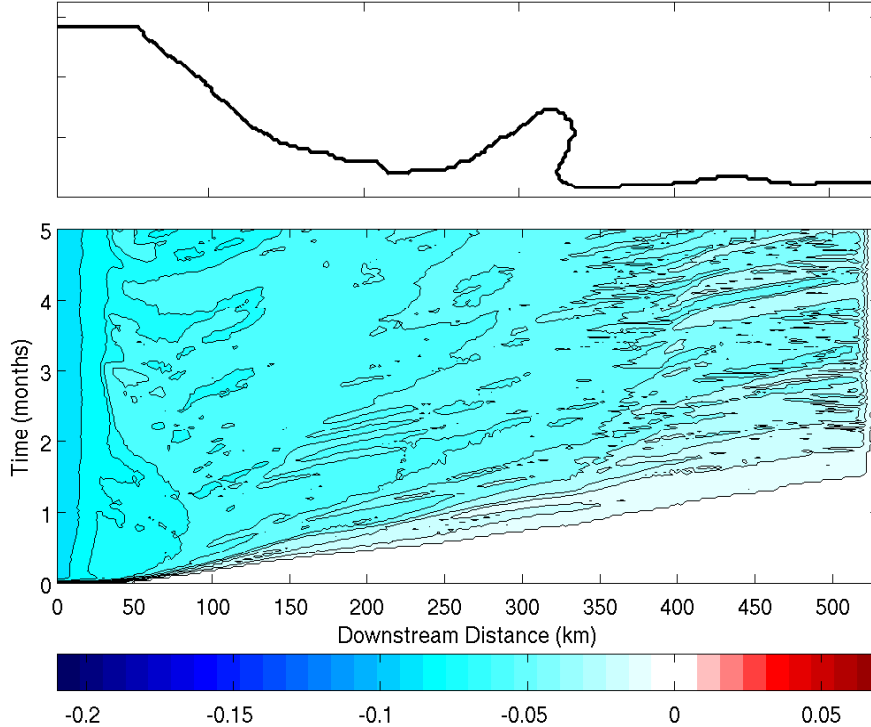
Fig. 21. Model coastal boundary (upper panel) and Hovmöller diagram versus downstream distance (lower panel) for the meridional WAC transport (Sv) of the base experiment.

sult the net volume of the $S \leq 38$ water increases during downwelling events. When winds weaken in the following days, this water keeps mixing and its volume decreases. This decrease is abruptly enhanced during the strong upwelling event. As in the idealized Sirocco cases, most of the freshwater mixes to form product water with salinity $S > 38$. The modalities of mixing seen in the idealized experiments are then respected for the rest of the period. $\Delta\mathcal{V}_{S \leq 38}$ increases early in the DART06b period when downwelling winds become predominant, and decreases in the last days of the period in the presence of upwelling winds. Since the trends are enhanced by the increased resolution, more freshwater is lost and the $\Delta\mathcal{V}_{S \leq 38}$ curve for the 0.5 km run is almost always below the 2 km one.

3.5 Meridional Transport

The Western Adriatic Current carries fresh water flowing along the Italian coast. According to different situations, the amount of fresh water moving southward is affected by winds, the presence of instabilities and mixing. It is

therefore useful to consider the meridional WAC transport, here defined as:

$$Tr_{WAC}(y,t) = \int\int v_{WAC}(x,y,z,t)\,dx\,dz\,,\qquad(2)$$

where

$$v_{WAC}(x,y,z,t) = \begin{cases} v(x,y,z,t)\,, & \text{if } S(x,y,z,t) \leq 38, \\ 0\,, & \text{otherwise}\,. \end{cases}$$

In the following, Hovmöller diagrams of Tr_{WAC} for the different experiments are shown. The x-axis is the downstream distance starting from the northern inflow boundary. In order to facilitate comprehension, the coastline profile has been added at the top of each figure.

In the baseline experiment (Fig. 21), fresh waters propagate downstream and reach the southern boundary of the domain after more than 1.5 months (shown by the zero-line transport). As evident in Fig. 5, instabilities, eddies, squirts and jets are created during this propagation. Ultimately all these processes are associated with mixing and with detrainment of water from the plume. Fig. 21 shows that, from a constant southward (negative) inflow at the northern boundary, transport values become gradually less negative moving downstream. Tr_{WAC} values are variable and noisy because of the presence of instabilities especially near the Gargano Promontory. Their advection downstream is responsible for the streaks of Fig. 21 parallel to the zero transport line. Note that the transport goes artificially back to zero in the last points due to the presence of the southern relaxation area.

Fig. 22 shows the Tr_{WAC} values for the fifteen days of idealized wind experiments. In the absence of wind, no difference is noted with respect to what was previously described in the baseline experiment. When Mistral winds blow, the southward WAC transport increases. This increase is not uniform and is larger in the mid-lower portion of the Adriatic. Here, waters with $S \leq 38$ are close to the Italian coast, and are soon forced to move meridionally due to the presence of the material boundary. In the northern part of the domain, instead, they can be found offshore and are free to move more zonally. At each point, the transport slightly decreases in time because of the mixing processes discussed in the previous paragraph.

Under Sirocco conditions, the WAC propagation is less regular than either in the absence of winds or under Mistral conditions. Surface waters along the Italian coast start flowing northward and topographically-trapped structures evolve and become evident. The southward freshwater transport starts to decrease, becomes null and ultimately reverses its sign. The transport values are influenced by the development of mesoscale recirculations. The area in the middle of the domain, all around the Gargano Promontory, remains initially clear from instabilities and the northward transport reaches its maximum after five days of persistent winds. The presence of these recirculations within the
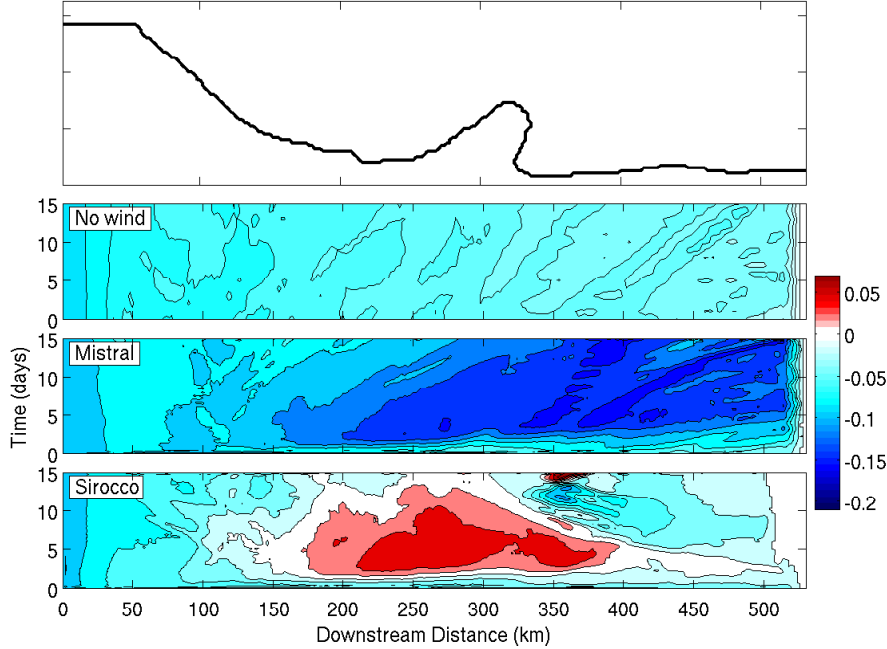
Fig. 22. Model coastal boundary (upper panel) and Hovmöller diagrams versus downstream distance (other panels) for the meridional WAC transport (Sv) of the idealized wind experiments.

coastal current, and the strong mixing happening under Sirocco conditions, reduce the alongshore freshwater transport in time.

Finally, Fig. 23 shows the Hovmöller diagram for the realistic experiment. On the right panel the meridional component of the wind stress averaged on the whole domain is plotted. The trends observed in the idealized experiments can be also recognized in this figure. However the wind sequence plays a crucial role in determining the Tr_{WAC} values. Different winds have to deal with the sea conditions left by the previous events. When winds are weak and not organized as until the end of August, the meridional transport remains southward and close to the low values registered in the no-wind case. A sudden increase in the southward transport corresponds to the strong Mistral event. In this case Tr_{WAC} values almost quadruple. When winds relax and are very weak, the coastal current starts to be characterized by different eddies all along the coast (as shown in Fig. 15) and the meridional transport decreases in magnitude and approaches zero. Positive local values appear during this time because weak southerly winds are present only along the Italian coast, but not in the rest of the domain (as for example in Fig. 15). Also in this case, there is little evidence of regular propagation. As in the idealized experiments, strong upwelling winds starting on September 13 are able to accelerate northward only the mid portion of the Adriatic, which is relatively clear of vortical structures. Afterwards, winds return to downwelling. They are not so strong as the ones at the end of August, but they last for a longer time. As a result the WAC transport once
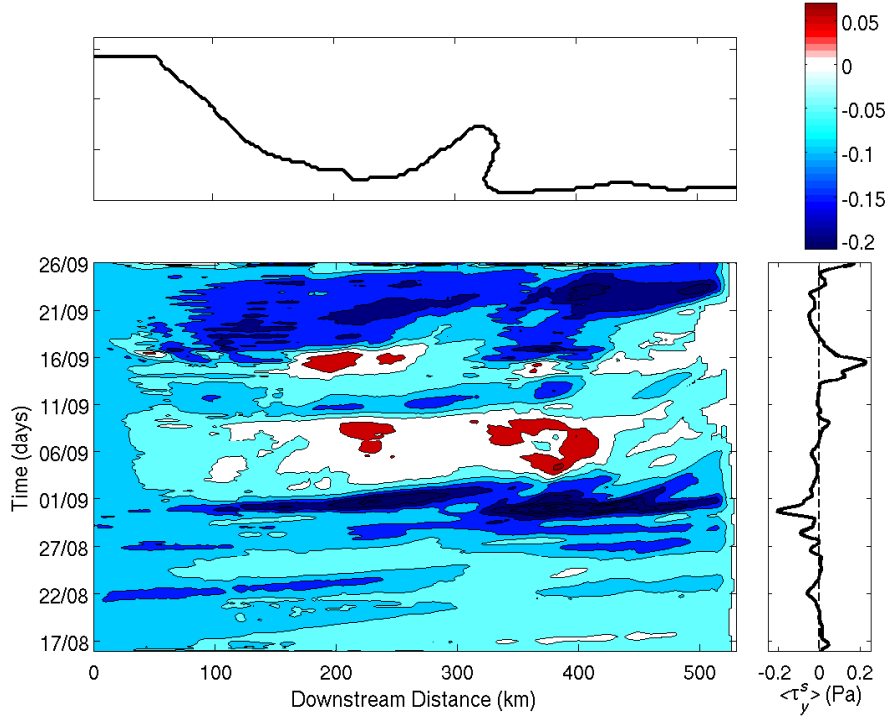
37

Fig. 23. Hovmöller diagram for the meridional WAC transport (Sv) for the realistic experiment.

again becomes southward and significant.

4   Conclusions

In this paper, a process study aimed at assessing the response of a turbulent buoyant current to wind forcing is presented. The case study is the Western Adriatic Current (Adriatic Sea), which is known to be characterized by strong mesoscale activity, and has recently been the focus of the Dynamics of the Adriatic Real Time project. Since the turbulent state of a buoyant current controls the transport and mixing of different substances, the results of this study are relevant for different practical applications. These include dispersion of pollutants, nutrients and sediments as well as floating organisms such as larvae of bivalves and commercial fish.

Data collected during the summer DART06b period are used to set up simulations which are only boundary, buoyancy and wind driven. Different simulations explore the turbulent variability under both idealized and more realistic wind conditions and for different horizontal resolutions. The idealized runs are based on the evidence that the averaged wind stress direction exhibits a strong bimodal distribution. The most frequent winds during DART06b, in

fact, blow from opposite directions and are downwelling or upwelling favorable. The differences in these cases are quantified in terms of mixing and along shore transport.

In the absence of wind the WAC is on average 15 m thick and 42 km wide. Flowing along the Italian coast, the current is forced to detach from the coastline, form instabilities and mix with the offshore denser fluid. Its southward transport gradually decreases with distance from the inflow boundary. In idealized downwelling conditions, the current is pushed toward the Italian coast, reaches thicknesses above 20 m, halves its width and rapidly increases its southward transport. Plume waters mix with ambient waters, but most of the product waters remain with salinity $S \leq 38$ and the current retains its fresh water signal. As a result of mixing, the WAC southward transport slightly decreases in time. Wave-like corrugations with horizontal dimension of about 10 km also appear within the coastal current. Since the WAC narrows down, these features cannot grow, and they ultimately fade away. It is worth noticing that the evolution of these features is resolution dependent, since in the 0.5 km run both their onset and disappearance are observed at earlier times than the 2 km run.

With idealized upwelling winds the current is pushed offshore and it becomes thinner and wider. Since it decelerates and reverses its direction, the WAC transport decreases and becomes northward. Strong lateral mixing is also observed and most of the product water has salinity $S > 38$. Mixing can therefore dilute the initial freshwater signal significantly. Furthermore, since water keeps detraining, the northward transport reduces with time. As soon as instabilities form, they can grow and form eddies with horizontal dimension of about 35 km. The presence of these recirculations further reduces the transport. The above trends remain the same when the 0.5 km run is considered.

The surface salinity fields of the realistic experiments qualitatively reproduce the state captured by the satellite Chl-a images. On the one hand, some of the trends observed in the idealized winds simulations are respected. For example, after strong downwelling events, like the one beginning on August 30, the WAC accelerates southward, shrinks and deepens, while a large amount of fresh water is still found along the Italian coast. It also appears more steady since the larger instabilities disappear. After strong upwelling events, like the one starting on September 13, the WAC accelerates northward and reverses its flow. It also becomes thinner and wider while larger instabilities and mixing ensue. As before, the total volume occupied by the $S \leq 38$ waters increases after Mistral winds, and strongly decreases after Sirocco ones. On the other hand, the sequence of events plays a crucial role. For example, the meridional transport in the realistic experiment is affected not only by the winds, but also by the state of the sea induced by the previous wind forcing. It is generally true that downwelling (upwelling) events correspond to an increase of the

southward (northward) transport. However, instabilities and recirculations set up by previous wind conditions strongly decrease this value. The more realistic high resolution simulation shows the same general qualitative trends of the low resolution case. However, the better detail in resolving turbulent features results in a strong quantitative difference with the coarser case for whit regard to mixing intensity (see section 3.4).

In this respect, the results highlight that attention must be paid to the models' horizontal resolution. Even if most operational Adriatic models are currently running at resolutions able to resolve the deformation radius (Zavatarelli and Pinardi, 2003; Cushman-Roisin et al., 2007; Martin et al., 2007), this study shows that mixing can be underestimated if $\Delta x > 0.5$ km. Furthermore, since the whole instability mechanism leading to the onset of smaller scale features is also resolution dependent, the same models may tend to delay the appearance of those instabilities as well as their disappearance.

The results also suggest that instabilities are generated by different mechanisms when winds blow from opposite directions. When Sirocco winds blow, eddy generation might be explained in terms of vorticity dynamics in the framework of baroclinic instabilities. Potential vorticity conservation can account for the generation of anticyclonic eddies, mainly due to the plume thinning under upwelling conditions. The horizontal dimension of the anticyclones is also several times the deformation radius, which agrees with the baroclinic instability theory (Pedlosky, 1987).

When Mistral winds blow, the wave-like irregularities remain small and the results indicate that a better theoretical understanding is needed in order to explain the genesis of those smaller instabilities. Even though there is some understanding of wind-induced frontogenesis in open ocean idealized scenarios (Thomas and Lee, 2005; Thomas and Ferrari, 2008), much is still left to do to understand coastal systems that are far from idealized flat bottom conditions. For example, it remains unclear how and exactly when instabilities develop when winds blow in presence of a material boundary, or over a realistic sloping bathymetry, and the coastal current or the Ekman layer can occupy the whole water column. The exact understanding of this mechanism requires the development of a dedicated set of numerical idealized experiments; a task which is left to future investigations.

Moreover, this work is limited to the DART06b summer period when Mistral and Sirocco winds are predominant. In other periods northeasterly Bora winds dominate in the Adriatic, and their spatial inhomogeneities are enough to induce instabilities (Bignami et al., 2007). Further investigations are necessary to assess this point.

Acknowledgements

A Appendix: Details on initial and boundary conditions

The initial salinity and temperature profiles are:

$$S(x, y, z, t = 0) = a_1^{ini} + a_2^{ini} \tanh\left(\frac{z + h_c^{ini}}{h_d}\right), \qquad \text{(A.1)}$$

$$T(x, y, z, t = 0) = b_1^{ini} + b_2^{ini} \tanh\left(\frac{z + h_c^{T}}{h_d}\right), \qquad \text{(A.2)}$$

where $h_c^{ini} = 25$ m, $h_c^T = 22$ m, $h_d = 5$ m,

$$a_1^{ini} = \frac{S^{srf} + S^{bot}}{2}, \qquad \text{(A.3)}$$

$$a_2^{ini} = a_1^{ini} - S^{bot}, \qquad \text{(A.4)}$$

$$b_1^{ini} = \frac{T^{srf} + T^{bot}}{2}, \qquad \text{(A.5)}$$

$$b_2^{ini} = b_1^{ini} - T^{bot}, \qquad \text{(A.6)}$$

and $S^{srf} = 38.3$, $S^{bot} = 38.5$, $T^{srf} = 23.5°$C and $T^{bot} = 13.0°$C.

At the northern (inflow) boundary, if X_N^{Ic} is the position of the Italian coast,

$S_N^{srf} = 38.1$, $X_0 = 8$ km and $L_d = 12$ km, the salinity field is relaxed to:

$$S(x = x_N, y, z, t) = a_1(x) + a_2(x) \tanh\left(\frac{z + h_c(x)}{h_d}\right), \qquad (A.7)$$

where if $x \geq X_N^{Ic} + X_0$

$$a_1(x) = \frac{S_N^{srf} + S^{bot}}{2} - \frac{\Delta S}{2} \exp\left(\frac{x - X_N^{Ic} - X_0}{L_d}\right), \qquad (A.8)$$

$$a_2(x) = a_1(x) - S^{bot}, \qquad (A.9)$$

$$h_c(x) = h_c^{ini} - \Delta h \exp\left(\frac{x - X_N^{Ic} - X_0}{L_d}\right), \qquad (A.10)$$

otherwise

$$a_1(x) = \frac{S_N^{srf} + S^{bot}}{2} - \frac{\Delta S}{2}, \qquad (A.11)$$

$$a_2(x) = a_1(x) - S^{bot}, \qquad (A.12)$$

$$h_c(x) = h_c^{ini} - \Delta h, \qquad (A.13)$$

and $\Delta S = 0.9$, $\Delta T = 1.75°C$ and $\Delta h = 13$ m.

References

Barale, V., Rizzoli, P. M., Hendershott, M. C., 1984. Remotely sensing the surface dynamics of the Adriatic Sea. Deep Sea Res. 31 (12), 1433–1459.

Batchelor, G., 1967. An Introduction to Fluid Dynamics. Cambridge University Press, 615 pp.

Bignami, F., Sciarra, R., Carniel, S., Santoleri, R., 2007. Variability of Adriatic Sea coastal turbid water from SeaWiFS imagery. J. Geophys. Res. 112, C03S10, doi:10.1029/2006JC003518.

Blanton, J. O., Oey, L. Y., Amft, J., Lee, T. N., 1989. Advection of momentum and buoyancy in a coastal frontal zone. J. Phys. Oceanogr. 19, 98–115.

Blumberg, A. F., Mellor, G. L., 1987. Three-dimensional coastal ocean models. American Geophysical Union, Ch. A description of a three-dimensional coastal ocean circulation model, p. 208 pp.

Book, J. W., Signell, R. P., Perkins, H., 2007. Measurements of storm and nonstorm circulation in the northern Adriatic: October 2002 through April 2003. J. Geophys. Res. 112, C11S92, doi:10.1029/2006JC003556.

Burrage, D. M., Book, J. W., Martin, P. J., 2009. Eddies and filaments of the Western Adriatic Current near Cape Gargano: analysis and prediction. J. Mar. Syst. In press, doi:10.1016/j.jmarsys.2009.01.024.

Canuto, V. M., Howard, A., Cheng, Y., Dubovikov, M. S., 2001. Ocean turbulence, Part I: one-point closure model momentum and heat vertical diffusivities. J. Phys. Oceanogr. 31, 1413–1426.

Capet, X., McWilliams, J. C., Molemaker, M. J., Shchepetkin, A. F., 2008a. Mesoscale to submesoscale transition in the California Current System. Part I: flow structure, eddy flux, and observational tests. J. Phys. Oceanogr. 38, 29–43.

Capet, X., McWilliams, J. C., Molemaker, M. J., Shchepetkin, A. F., 2008b. Mesoscale to submesoscale transition in the California Current System. Part II: frontal processes. J. Phys. Oceanogr. 38, 44–64.

Chanut, J., Barnier, B., Large, W., Debreu, L., Penduff, T., Molines, J. M., Mathiot, P., 2008. Mesoscale eddies in the Labrador Sea and their contribution to convection and restratification. J. Phys. Oceanogr. 38, 1617–1643, doi:10.1175/2008JPO3485.1.

Chao, S.-Y., 1987. Wind-driven motion near inner shelf fronts. J. Geophys. Res. 92, 3849–3860.

Chao, S.-Y., 1988. Wind-driven motion of estuarine plumes. J. Phys. Oceanogr. 18, 1144–1166.

Chapman, D. C., Lentz, S. J., 1994. Trapping of a coastal density front by the bottom boundary layer. J. Phys. Oceanogr. 18, 1464–1479.

Chiggiato, J., Oddo, P., 2008. Operational ocean models in the Adriatic Sea: a skill assessment. Ocean Sci. 4, 61–71.

Cushman-Roisin, B., Gačić, M., Poulain, P. M., Artegiani, A., 2001. Physical oceanography of the Adriatic Sea: past, present and future. Kluwer Academic Publishers, 320 pp.

Cushman-Roisin, B., Korotenko, K. A., 2007. Mesoscale-resolving simulation of summer and winter bora events in the Adriatic Sea. J. Geophys. Res. 112, C11S91, doi:10.1029/2006JC003516.

Cushman-Roisin, B., Korotenko, K. A., Galos, C. E., Dietrich, D. E., 2007. Simulation and characterization of the Adriatic Sea mesoscale variability. J. Geophys. Res. 112, C03S14, doi:10.1029/2006JC003515.

Dong, C., McWilliams, J. C., 2007. A numerical study of island wakes in the Southern California Bight. Cont. Shelf Res. 27, 1233–1248.

Dong, C., McWilliams, J. C., Shchepetkin, A. F., 2007. Island wakes in deep water. J. Phys. Oceanogr. 37, 962–981, doi:10.1175/JPO3047.1.

Flather, R., 1976. A tidal model of the northwest European continental shelf. Mem. Soc. R. Sci. Liege 6 (10), 141–164.

Fong, D. A., Geyer, W. R., 2001. Response of a river plume during an upwelling wind event. J. Geophys. Res. 106 (C1), 1067–1084.

Fong, D. A., Geyer, W. R., Signell, R. P., 1997. The wind-forced response of a buoyant coastal current: observation of the Gulf of Maine plume. J. Mar. Syst. 12, 69–81.

Harrison, D. E., Robinson, A. R., 1978. Energy analysis of open regions of turbulent flows: mean eddy energetics of a numerical ocean circulation experiment. Dyn. Atmos. Oceans 2, 185–211.

Jackett, D. R., McDougall, T. J., 1995. Minimal adjustment of hydrostatic profiles to achieve static stability. J. Atmos. Oceanic Technol. 12 (2), 381–389.

Korotenko, K. A., 2007. Modeling the mesoscale variability in the Adriatic Sea. Oceanology 47 (3), 313–324.

Kourafalou, V. H., Oey, L. Y., Wang, J. D., Lee, T. N., 1996. The fate of river discharge on the continental shelf 1. Modeling the river plume and the inner shelf coastal current. J. Geophys. Res. 101, 3415–3434.

Lentz, S. J., 2001. The influence of stratification on the wind-driven cross-shelf circulation over the North Carolina shelf. J. Phys. Oceanogr. 31, 2749–2760.

Lentz, S. J., Helfrich, K. R., 2002. Buoyant gravity currents along a sloping bottom in a rotating fluid. J. Fluid Mech. 464, 251–278.

Lentz, S. J., Largier, J., 2006. The influence of wind forcing on the Chesapeake Bay buoyant coastal current. J. Phys. Oceanogr. 36, 1305–1316.

Lutjeharms, J. R. E., Penven, P., Roy, C., 2003. Modelling the shear edge eddies of the southern Agulhas Current. Cont. Shelf Res. 23, 1099–1115.

Magaldi, M. G., Özgökmen, T. M., Griffa, A., Chassignet, E. P., Iskandarani, M., Peters, H., 2008. Turbulent flow regimes behind a coastal cape in a stratified and rotating environment. Ocean Modell. 25, 65–82, doi:10.1016/j.ocemod.2008.06.006.

Martin, P. J., Book, J. W., Burrage, D. M., Rowley, C. D., Tudor, M., 2009. Comparison of model-simulated and observed currents in the central Adriatic during DART. J. Geophys. Res. 114, C01S05, doi:10.1029/2008JC004842.

Martin, P. J., Book, J. W., Doyle, J. D., 2007. Simulation of the northern Adriatic circulation during winter 2003. J. Geophys. Res. 112, C03S12, doi:10.1029/2006JC003511.

Münchow, A., Garvine, R. W., 1993. Buoyancy and wind forcing of a coastal current. J. Mar. Res. 51, 293–322.

Oddo, P., Pinardi, N., Zavatarelli, M., 2006. A numerical study of the inter-annual variability of the Adriatic Sea (20002002). Sci. Total Environ. 353, 39–56.

O'Reilly, J. E., Maritorena, S., Mitchell, B. G., Siegel, D. A., Carder, K. L., Garver, S. A., Kahru, M., McClain, C., 1998. Ocean color chlorophyll algorithm for SeaWiFS. J. Geophys. Res. 103, 24937–24953.

Pasarić, Z., Belušić, D., Chiggiato, J., 2009. Orographic effects on meteorological fields over the Adriatic from different models. J. Mar. Syst. In press, doi:10.1016/j.jmarsys.2009.01.019.

Paschini, E., Artegiani, A., Pinardi, N., 1993. The mesoscale eddy field of the Middle Adriatic Sea during fall 1988. Deep Sea Res. 40 (7), 1365–1377.

Pedlosky, J., 1987. Geophysical Fluid Dynamics, 2nd Ed. Spinger-Verlag, 710 pp.

Poulain, P.-M., 2001. Adriatic Sea surface circulation as derived from drifter data betwee 1990 and 1999. J. Mar. Syst. 29, 3–32.

Poulain, P.-M., Mauri, E., Ursella, L., 2004. Unusual upwelling event and

current reversal off the Italian Adriatic coast in summer 2003. Geophys. Res. Lett. 31, L05303, doi:10.1029/2003GL019121.

Rixen, M., Book, J., Carta, A., Grandi, V., Gualdesi, L., Stoner, R., Ranelli, P., Cavanna, A., Zanasca, P., Baldasserini, G., Trangeled, A., Lewis, C., Trees, C., Grasso, R., Giannechini, S., Fabiani, A., Merani, D., Berni, A., Leonard, M., Martin, P., Rowley, C., Hulbert, M., Quaid, A., Goode, W., Preller, R., Pinardi, N., Oddo, P., Guarnieri, A., Chiggiato, J., Carniel, S., Russo, A., Tudor, M., Lenartz, F., Vandenbulcke, L., 2009a. Improved ocean prediction skill and reduced uncertainty in the coastal region from multi-model super-ensembles. J. Mar. Syst. In press, doi:10.1016/j.jmarsys.2009.01.014.

Rixen, M., Book, J., Orlic, M., 2009b. Coastal processes: challenges for monitoring and prediction. Preface. J. Mar. Syst. In press, doi:10.1016/j.jmarsys.2009.01.006.

Schlichting, H., Gersten, K., 2003. Boundary Layer Theory. Spinger-Verlag, 801 pp.

Shchepetkin, A. F., McWilliams, J. C., 1998. Quasi-monotone advection schemes based on explicit locally adaptive dissipation. Mon. Weather Rev. 126 (6), 1541–1580.

Shchepetkin, A. F., McWilliams, J. C., 2005. The regional oceanic modeling system (ROMS): a split-explicit, free-surface, topography-following-coordinate oceanic model. Ocean Modell. 9 (4), 347–404.

Silva, M., Araujo, M., Servain, J., Penven, P., Lentini, C. A. D., 2009. High-resolution regional ocean dynamics simulation in the southwestern tropical Atlantic. Ocean Modell. 30, 256–269.

Smolarkiewicz, P. K., 1984. A fully multidimensional positive definite advection transport algorithm with small implicit diffusion. J. Comput. Phys. 54, 325–362.

Sur, H. İ., Özsoy, E., Ünlûata, Ü., 1994. Boundary current instabilities, upwelling, shelf mixing and eutrophication in the Black Sea. Prog. Oceanog. 33, 249–302.

Thomas, L. N., Ferrari, R., 2008. Friction, frontogenesis, frontal instabilities and the stratification of the surface mixed layer. J. Phys. Oceanogr. 38, 2501–2518.

Thomas, L. N., Lee, C. M., 2005. Intensification of ocean fronts by down-front winds. J. Phys. Oceanogr. 35, 1086–1102.

Umlauf, L., Burchard, H., 2003. A generic length-scale equation for geophysical turbulence models. J. Marine Res. 61, 235–265.

Veneziani, M., Griffa, A., Poulain, P.-M., 2007. Historical drifter data and statistical prediction of particle motion: a case study in the central Adriatic Sea. J. Atmos. Ocean. Tech. 24, 235–254, doi:10.1175/JTECH1969.1.

Vetrano, A., Gačić, M., Kovačević, V., 1999. Water fluxes through the Strait of Otranto. Ecosystem Research Report 32, European Commission.

Whitney, M. M., Garvine, R. W., 2005. Wind influence on a coastal buoyant outflow. J. Geophys. Res. 110, C03014, doi:10.1029/2003JC002261.

Xing, J., Davies, A. M., 1999. The effects of wind direction and mixing upon

the spreading of a buoyant plume in a non-tidal regime. Cont. Shelf Res. 19, 1437–1483.

Yankovsky, A. E., Chapman, D. C., 1997. A simple theory for the fate of buoyant coastal discharges. J. Phys. Oceanogr. 27, 1386–1401.

Zavatarelli, M., Pinardi, N., 2003. The Adriatic Sea modelling system: a nested approach. Ann. Geophys. 21, 345–364.